

# UC Davis

## UC Davis Electronic Theses and Dissertations

### Title

Multi-directional Loading of 3D-Printed Tree Root Models using a Six-Axis Robotic Arm

### Permalink

<https://escholarship.org/uc/item/0kf0m954>

### Author

Miller, Jasmine Victoria

### Publication Date

2021

Peer reviewed|Thesis/dissertation

Multi-directional Loading of 3D-Printed Tree Root Models using a Six-Axis Robotic Arm

By

JASMINE MILLER  
THESIS

Submitted in partial satisfaction of the requirements for the degree of

MASTER OF SCIENCE

in

Civil & Environmental Engineering

in the

OFFICE OF GRADUATE STUDIES

of the

UNIVERSITY OF CALIFORNIA

DAVIS

Approved:

---

Alejandro Martinez

---

Jason DeJong

---

Junliang Tao

Committee in Charge

2021

---

*Dedicated to my family and my life partner, Gerry*

---

## Acknowledgements

Many supported me and the work I present in this thesis. I would like to give some individual notes of gratitude to those many.

I first want to thank my advisor, Dr. Alejandro Martinez. He believed I had potential before I believed it. He supported me through the trials and tribulations of being a graduate student in the midst of COVID-19. He was patient and helped guide me when I needed it most. Best of all, he passed on to me his two guinea pigs, Pantufla (RIP) and Francesca, who were/have been wheeking lights of joy while I worked from home.

A show of gratitude is deserved for my thesis committee members Dr. Jason DeJong and Dr. Junliang Tao for their knowledge and insight on my work. A huge thanks goes to my peers in GGSS (Geotechnical Graduate Student Society). Thanks to Mandeep Basson for always offering a helping hand, to Olivia Hunt for embarking on the journey of grad school with me, and to Kyle O'Hara, Yuyan Chen, and Lin Huang for helping me with miscellaneous work and advice.

I would also like to thank all of my professors at UC Davis for working with me to ensure that I had the best chance at succeeding in their courses.

This material is based upon work supported by the Engineering Research Center Program of the National Science Foundation (NSF) under NSF Cooperative Agreement EEC-1449501. Any opinions, findings and conclusions or recommendations expressed in this material are those of the authors and do not necessarily reflect those of the NSF. I would also like to acknowledge the funding and support I received from CBBG (Center for Bio-mediated and Bio-inspired Geotechnics).

---

I want to thank friends and family for their support throughout my master's experience. Thank you to my friend Julia Tse for always remembering to reach out and visit me even though you had to drive far. Thanks to Giovanna Zuniga, Holly Davis, and Jenna Zaleski for sticking by my side for over a decade. Thanks to my parents, Veronica and Matt Miller, and my five brothers, Michael, Nathan, Steven, David, and Adam for being there when I need it most and for making me smile. I am forever grateful for my partner, Gerardo "Gera" or "Gerry" Ochoa for being my steady rock through everything, and for making meals for me, helping around the house, and being my COVID-19 isolation buddy.

I couldn't go without mentioning my pets. To my bearded dragon, Pepina "Nina", for being the best first pet a person could ask for. To my dog, Maggie, for being a little turd nugget. Rest in Peace to Paprika and Pantufla (guinea pigs). And to all the other guineas: Francesca "Frankie", Alice, and Emily. Honorable mention to Tuck, the little turtle that could.

---

Jasmine Miller

September 2021

Civil and Environmental Engineering

**MULTI-DIRECTIONAL LOADING OF 3D-PRINTED TREE ROOT MODELS USING A SIX-AXIS  
ROBOTIC ARM**

**Abstract**

The application of bio-inspiration in geotechnical engineering can help develop more efficient and effective solutions. Biological processes, such as the growth of tree roots, have evolved to accommodate limited resources for growth. Recent work provides evidence that root systems can have a significantly higher axial load capacity per material unit mass or volume than conventional foundation systems such as micropiles. For the work presented in this thesis, two small scale root-inspired models (6-leg and 3-leg), a pile, and a plate anchor were 3D printed and tested under combined loading conditions. The tests were performed using a six-axis robotic arm at 1g in subrounded, loose sand. The results of these tests were compared to assess the performance of the tree root-inspired models relative to more standard shapes. In both vertical and horizontal pullout, the piles had the lowest absolute pullout resistance and the plate anchors the highest. The results showed the mobilization of peak capacities at smaller displacements as the pullout angle became more vertical. After normalizing the results by volume, the tests indicate a greater material efficiency in the tree root model with 6 legs relative to the plate, the pile, and the 3 leg models for most directions of loading. The pile gradually increased peak capacity as the pullout angle approached horizontal, nearly matching in material efficiency with the 6-leg model for the horizontal load test. The results suggest that tree-root inspired shapes may provide anchorage with

---

lower material use than traditional practice. In addition, the results of this study show that 1g tests using a robotic arm be used to explore the behavior of soil-structure interaction problems.

---

## Table of Contents

Acknowledgements	iii
Abstract	v
List of Tables	ix
List of Figures	x
Chapter 1 Introduction	1
Chapter 2 The behavior of tree roots and tree root analogues under applied loading	3
2.1 Background	3
2.2 Root parameters	3
2.2.1 Tree root types	4
2.2.2 Root system architecture	6
2.3 Vertical pullout capacity	9
2.3.1 Force distribution and failure mechanisms	9
2.3.2 Root material	11
2.3.3 Root architecture	15
2.4 Lateral and moment capacity	20
2.4.1 Number and presence of laterals and sub-laterals	20
2.4.2 Combined loading	21
Chapter 3 Ultimaker S5: Building a Model	22
3.1 Equipment Information	22
3.2 Software Set-up	22
3.2.1 3D Modeling software	22
3.2.2 Ultimaker Cura	23
3.3 Material selection	25
3.3.1 Commonly used materials and their properties	25
3.3.2 Support materials	25
3.3.3 Tree root model material combination	27
3.4 Printing Procedure	28
3.4.1 Pre-print procedure	28
3.4.2 Post-print procedure	30
3.5 Common Issues	31
3.5.1 Humidity	32

---

3.5.2	Low filament extrusion	33
3.6	Final Printed Parts	34
Chapter 4	Universal Robots UR16e	36
4.1	Equipment Information	36
4.2	Teaching Pendant: Using Polyscope	37
4.2.1	Password Protections	37
4.2.2	Tool Configuration	38
4.2.3	Writing a program	39
4.3	Communicating with the UR16e and the Axia F/T Sensor	43
4.3.1	Ethernet Connection	43
4.3.2	Communication with UR16e	44
4.3.3	Communication with Axia F/T Sensor	45
4.4	Robotic Arm Testing Alignment	47
4.4.1	Robotic arm position	47
4.5	Data Post-processing	48
4.5.1	Zeroing the data	48
4.5.2	Identifying the cutoff displacement	49
4.5.3	Calculating horizontal and vertical force data	49
4.5.4	Data filtration	51
Chapter 5	Results and Analysis	52
5.1	Vertical and Horizontal Loading	52
5.1.1	Materials and methods	52
5.1.2	Load versus displacement curves for anchor load tests	53
5.1.3	Vertical vs. horizontal load	59
5.1.4	Peak loads	65
5.2	Loading Efficiency	69
5.2.1	Volume normalized peak load	69
5.2.2	Vertical capacity comparison	71
5.2.3	Horizontal Capacity Comparison	75
5.2.4	Resultant capacity comparison	78
Chapter 6	Conclusions	81
References		84

---

---

## LIST OF TABLES

Table 2.1: Failure mechanisms observed by (Hamza, Bengough and Bransby) and hypothesized causes of failure .....	10
Table 2.2: Definition of variables for Equations 2.1 and 2.2.....	14
Table 3.1: Useful links for 3D printing.....	24
Table 3.2: Settings to print clean print in Ultimaker S5 .....	26
Table 3.3: Ultimaker material advantages and disadvantages ( <a href="http://core-electronics.com/au">core-electronics.com/au</a> ) .....	27
Table 3.4: Procedure to load filament spools.....	29
Table 3.5: Model dimensions.....	35
Table 4.1: Discretization of data into vertical and horizontal direction. ....	50
Table 5.1: Properties of Ottawa F-65 (Palumbo).....	52
Table 5.2: Model volumes .....	69

---

## LIST OF FIGURES

Figure 2.1: Typical tree root types: (A) the tap root, (B) the lateral roots, (C) deeply descending roots, and (D) fibrous roots (Menashe, 2004).....	4
Figure 2.2: First set of laterals (upper layer) versus second set of laterals (lower layer) (Perry, 1989).....	5
Figure 2.3: Herringbone and dichotomous branching topologies (Bouma, Nielsen, Van Hal, & Koutstaal, 2001).....	7
Figure 2.4: Branch angles $\alpha$ and $\theta$ .....	8
Figure 2.5: Load versus displacement curve for analogue (Mickovski, Benough, Bransby, Davis, & Hallett, 2007) .....	12
Figure 2.6: Interface shear test results for (a) wood-sand interface and (b) rubber-sand interface (Mickovski, Bransby, Bengough, Davies, & Hallett, 2010).....	13
Figure 2.7: Fractal plate designs for model anchors (Dyson & Rognon, 2014).....	15
Figure 2.8: Schematic of all types of model roots tested in Stokes et al. (1996).....	17
Figure 2.9: Force diagram on tree root system under lateral loading (Coutts, 1989).....	20
Figure 2.10: Multi-directional failure envelope for circular plate foundation on uniform soil with no bonding at the foundation-soil interface (Gourvenec, 2007).....	21
Figure 2.11: Multi-directional failure envelope for circular plate foundation on uniform soil with no bonding at the foundation-soil interface (Gourvenec, 2007).....	21
Figure 3.1: Ultimaker Cura base setting interface (support.ultimaker.com) .....	23
Figure 3.2: Successful model print layout .....	24
Figure 3.3: Ultimaker PVA, damaged by humidity.....	32
Figure 3.4: 3D-printed filament spool holder .....	33
Figure 3.5: From left to right: Model holder for use during sand pluviation, the four selected models for testing, and the tool connector used to attach the model to the robotic arm.....	34
Figure 4.1: Robotic arm parts diagram (not pictured are the control box and the Teaching Pendant).....	36
Figure 4.2: Coordinate systems of the tool (red dot) and the base (blue dot).....	40
Figure 4.3: Example program written to move the robot between five waypoints.....	43
Figure 4.4: Ethernet connection system for UR16e and Axia F/T sensor. ....	44
Figure 4.5: Lines of code in the RTDE “record.py” file that are relevant for connecting to the robot.....	45
Figure 4.6: Control board cable arrangement to power the Axia F/T sensor .....	46
Figure 4.7: Assembly of parts used to connect the robotic arm to the model.....	47
Figure 4.8: Robotic arm test alignment.....	48

---

Figure 4.9: Directionality of load cell data relative to test alignment .....	48
Figure 4.10: Unfiltered vs. filtered load vs. displacement data .....	51
Figure 5.1: Pluviator used in testing .....	53
Figure 5.2: Force versus displacement for the pile model showing force in the vertical-, horizontal-, and z-direction .....	55
Figure 5.3: Force versus displacement for the plate model showing force in the vertical-, horizontal-, and z-direction.....	56
Figure 5.4: Force versus displacement for the 6-leg model showing force in the vertical-, horizontal-, and z-direction.....	58
Figure 5.5: Force versus displacement for the 3-leg model showing force in the vertical-, horizontal-, and z-direction.....	59
Figure 5.6: Vertical versus horizontal load for the pile model. Failure envelope is drawn in orange. ....	61
Figure 5.7: Vertical versus horizontal load for the plate model. Failure envelope is drawn in orange. ....	62
Figure 5.8: Vertical versus horizontal load for the 6-leg model. Failure envelope is drawn in orange.....	63
Figure 5.9: Vertical versus horizontal load for the 3-leg model. Failure envelope is drawn in orange.....	64
Figure 5.10: Failure envelopes for the four models.....	64
Figure 5.11: Peak force for each model in the vertical-, horizontal-, resultant-, and z-directions	66
Figure 5.12: Volume normalized peaks for vertical-, horizontal-, resultant-, and z-direction for the tested models.....	70
Figure 5.13: Vertical peak loads for each angle compared between models.....	73
Figure 5.14: Vertical, volume normalized peak loads for each angle compared between models	74
Figure 5.15: Horizontal peak loads for each angle compared between models.....	76
Figure 5.16: Horizontal, volume normalized peak loads for each angle compared between models .....	77
Figure 5.17: Resultant peak loads for each angle compared between models.....	79
Figure 5.18: Resultant, volume normalized peak loads for each angle compared between models .....	80

---

**CHAPTER 1 INTRODUCTION**

Bio-inspired design begins with the observation of a naturally occurring process. A hypothesis is built to suggest the application of the naturally occurring process in a human-made design. Tree roots have long been studied in many disciplines to assess how they function, what makes them grow at different rates, what direction they grow and why, and how to anticipate or prevent their failure in the case of heavy loads on the tree or from the tree's mass. The focus of this thesis is to utilize the current understanding of tree root behavior to investigate the behavior of tree root inspired anchors.

Tree roots have two primary functions, nutrient uptake and anchorage. This work hypothesizes that tree roots are material efficient in their anchorage capabilities because they often grow in resource deficient environments. There could be many reasons for this material efficiency, one of which is tree root architecture (i.e. the geometry of the root system and the individual roots).

In this work, simplified tree root models are fabricated and tested to evaluate how tree root architecture affects the behavior and capacity of anchors subjected to multi-directional loading. The models are simplified to help isolate the factors within tree root architecture that may affect pullout behavior. To assess a broader scope of model behavior under loading, the tests are performed by pulling the models out vertically, horizontally, and at angles between the two extremes.

Because of their complex shape, the models are constructed using a 3D printer, the Ultimaker S5. The 3D-printer can print intricate models with consistent material properties between prints. To perform tests at varied angles, a robotic arm is used, the UR16e, in conjunction with an external, six-axis load cell, the Axia80-m20 F/T sensor. Part of this work assesses the feasibility of using a

3D-printer and a robotic arm to investigate a soil-structure interaction problem in a 1g laboratory setting.

The results of this work are used to prove or disprove the hypothesis that tree root shapes can be more material efficient than traditional models, such as the pile and plate anchor. The shape of the tree root models depends on which tree root architecture attribute to isolate. Traditional models are also printed and used to compare against the tree root shapes.

If the hypothesis proves to be true for this testing sequence, the research will not only prompt reason for further study but will hopefully foreshadow the application of this work in the field. The tree root shape can be applied to the shape of anchors and piles. Tree root shapes may help reduce material costs and decrease the environmental impact of the construction of anchors and pile foundations.

This thesis consists of the following five additional chapters:

- Chapter 2: This includes a synopsis of previous work related to tree root architecture and anchorage capacity.
- Chapter 3: This includes details about the 3D-printer used for testing. Guidance for how to use the printer is included.
- Chapter 4: This includes details about the robotic arm used for testing. Instructions for how to use the robotic arm as well as how to use the external load cell are described.
- Chapter 5: This includes the results and analysis from the testing performed with the 3D-printed models and the robotic arm. Graphics of the results are included to help understand the conclusions and comparisons made.

## **CHAPTER 2 THE BEHAVIOR OF TREE ROOTS AND TREE ROOT ANALOGUES UNDER APPLIED LOADING**

### **2.1 BACKGROUND**

Both tree roots and smaller plant roots, also called herbaceous species, have been used in previous research to analyze the anchorage capacity of root systems. As noted in Coutts (1989), the distinction between these two root types may have a large effect on the formation and function of the root system. Herbaceous plant species may be optimized for seasonal or annual life cycles whereas tree roots must grow to provide structural support and nutrient storage and transport for decades (Coutts, 1989). Because of this notable difference, tree roots may be the preferred reference for optimizing root anchorage based on root system properties. Research on the anchorage of herbaceous roots is included as a comparative tool against tree root and model root testing with the understanding that the growth of herbaceous roots may not be optimized for anchorage. The properties relevant to this research includes root type, architecture, material, and behavior under loading and failure conditions. This review focuses on root capacity subjected to vertical loading. However, a brief description of the behavior of roots subjected to lateral and combined loading is also provided.

### **2.2 ROOT PARAMETERS**

The primary functions of tree roots are to provide anchorage for the tree and to transport water and nutrients from the soil to the main tree stem. Tree roots are structures with complex architecture and variability in their growth patterns and material composition. Their unique properties have historically been characterized by root type and root architecture (Fitter, 1987). These categories help to analyze the relationship between root parameters, the surrounding soil parameters, and root functionality.

### 2.2.1 Tree root types

Tree roots are typically comprised of four main types, including a tap root, lateral roots, fibrous roots, and deeply descending roots as shown in Figure 2.1. The work of Thomas O. Perry in his 1989 paper “Tree Roots: Facts and Fallacies” helps to define root types in the following sections. The description of each tree root type does not imply that all trees have all mentioned root types. Instead, the following description is to highlight the key components of most trees.

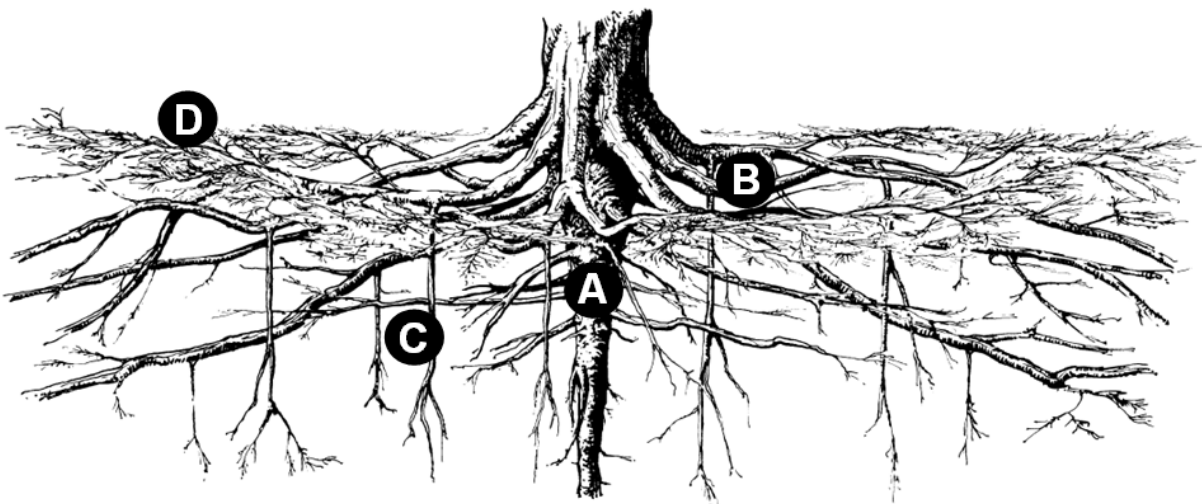


*Figure 2.1: Typical tree root types: (A) the tap root, (B) the lateral roots, (C) deeply descending roots, and (D) fibrous roots (Menashe, 2004)*

#### 2.2.1.1 Taproot

The taproot is the first root to grow from a seedling. Taproots are the largest root on a tree, with possible diameters greater than 30 centimeters (Perry, 1989). For some trees, such as willows and poplars, the taproot does not grow large enough to persist as a structural support member. For the trees that have a persisting taproot, such as pines and oaks, the root typically grows and tapers downward one to two meters as lateral roots grow and extend away from the taproot.

### 2.2.1.2 Lateral roots

Lateral roots, also called transport roots, are smaller in diameter than the taproot and grow horizontally away from the main stem (i.e. vertical axis through the tree trunk). Anywhere from four to eleven major first-order lateral roots extend from the main stem. First-order laterals usually form and grow radially outward in shallow ground, often causing near-surface swelling of the main trunk at the root offshoot point (i.e. point of dichotomy) (Perry, 1989).

The first set of laterals are usually in the top 20 - 30 centimeters of soil. Major laterals can extend one to four meters away from the main stem and have diameters ranging from 1 to 2.5 centimeters. Similar to the taproot, first-order laterals have decreasing diameter as they grow away from the main stem. Taproot and first-order laterals are typically comprised of woody material that grows in rings, similar to a tree trunk (Perry, 1989). A second layer of laterals can form at greater depth, as shown in Figure 2.2. The second set of first-order laterals branches off the taproot and striker roots at a depth just above soil with insufficient oxygen levels to support root growth (Perry, 1989).

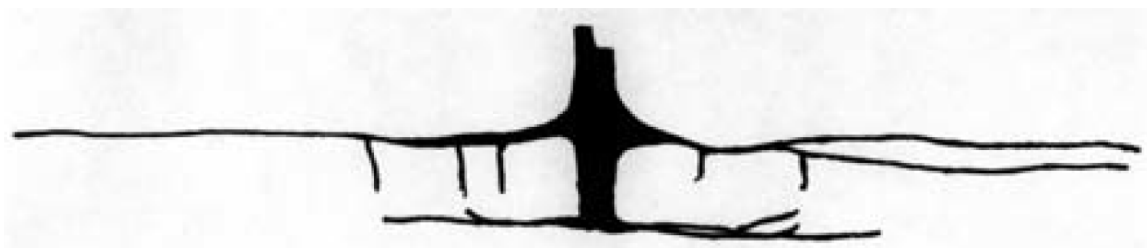


*Figure 2.2: First set of laterals (upper layer) versus second set of laterals (lower layer) (Perry, 1989)*

### 2.2.1.3 Deeply descending “striker/sinker” roots

Striker roots, like fibrous roots, grow from either the taproot or the first-order laterals. Striker roots grow downward, stopping or growing around obstructions encountered until they reach insufficient oxygen levels. As observed by Perry (1989), striker roots can be

considered transport roots since their primary function is to store and transfer water and nutrients to their parent branch. Coutts (1989) suggests that striker roots may also be important to developing anchorage.

#### 2.2.1.4 Fibrous roots

Of the four root types discussed, fibrous roots are the smallest and are the only “non-woody” roots. Schnelle et al. (1989) concluded that fibrous roots provide negligible anchorage. Their primary function is to absorb water and minerals (Schnelle, Feucht, & Klett, 1989). Fibrous roots branch off all other root types. Some fibrous roots, called root hairs, grow off another root and act to increase the absorptive surface area of a root (Perry, 1989).

### **2.2.2 Root system architecture**

Root system architecture is comprised of multiple measurable parameters such as root topology, branching angles, root lengths, and root diameters.

#### 2.2.2.1 Root topology

Much of the referenced literature for root topologic descriptions focuses on the causal relationship between resource availability and root topology. The relationship between root topology and anchorage will be explored in Section 2.3 and Section 2.4.

Root topology describes the pattern of root branching. Root topology types are simplified models characterized in biological literature to examine the nutrient uptake capacity and anchorage capacity of root systems. The two most discussed topologies are dichotomous and herringbone, shown in Figure 2.3. In Figure 2.3, the M parameter represents the magnitude of the root system which is defined by the number of free-ended roots. The A parameter is the altitude of the root system. The altitude is quantified by adding the number

of links (i.e. points of dichotomy) along the longest path from root base to free-ended roots. Intermediate links characterize the branch order, where the first order laterals stem from the first point of dichotomy off the main stem, the second order laterals branch off the first order laterals, and so on.

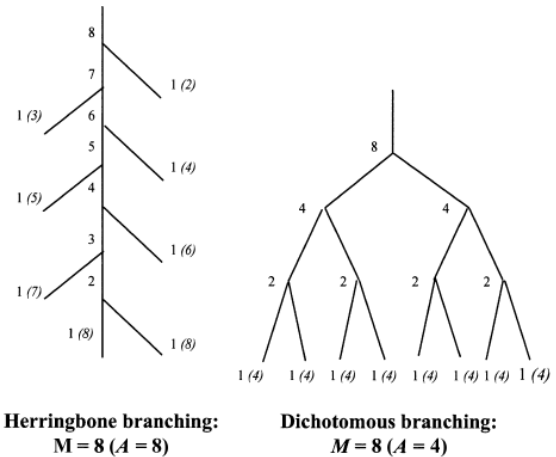


Figure 2.3: Herringbone and dichotomous branching topologies (Bouma, Nielsen, Van Hal, & Koutstaal, 2001)

Herringbone and dichotomous topologies

represent the opposing ends of the topology spectrum, with most topologies lying at or between each type.

Fitter et al. (1991) developed a computer program to simulate the relationship between the root topology and exploitation efficiency. Exploitation efficiency is defined as the ratio of the volume of soil in depletion zones to the volume of the root system. Depletion zones are soil volumes in which resource depletion can occur, where resources can be water, oxygen, and/or nutrients (Fitter, Stickland, & Harvey, 1991). The results of the model were described using the herringbone and dichotomous topologies.

### 2.2.2.1.1 Herringbone

Herringbone branching is characterized by few higher order laterals, shorter higher order laterals, and a deep taproot. The model by Fitter et al. (1991) suggests that herringbone branching formation occurs where there is a resource deficiency. Bouma et al. 2001 tested the model by Fitter et al. 1991 on salt marsh dicots grown in different resource availability environments. Low marshland vegetation growth was constrained by anoxic soil conditions. High marshland vegetation growth was constrained by

nutrient deficiency. The results suggest that the herringbone topology minimizes oxygen leakage and exposure to phytotoxins, making the herringbone topology ideal for anoxic soil conditions. The herringbone structure is also hypothesized to minimize competition of resource uptake between roots on the same system, which is beneficial in more root dense soils (Bouma, Nielsen, Van Hal, & Koutstaal, 2001).

#### 2.2.2.1.2 *Dichotomous*

For dichotomous branching, the order of laterals increases with depth due to the formation of multiple laterals from the ends of each parent lateral. Minimal to no taproot exists for a dichotomous branching system. Contrastingly to herringbone branching, the model by Fitter et al. (1991) suggests that dichotomous branching topology allows for a higher nutrient intake capacity than herringbone, making a dichotomous topology ideal for nutrient rich conditions in near surface soils. Some of the dicots tested by Bouma et al. (2001) behaved accordingly with this hypothesis, where deviation from the hypothesis may have been a result of the plant species tested and the similar nutrient deficiencies in both low and high marshland.

#### 2.2.2.2 Root angles

Roots grow away from their parent stems at a variety of different angles. The reasons for these varying angles may include the original orientation of growth, pull of gravity, nutrient distribution in the soil, presence of mechanical barriers (such as rocks or dense soil), and more (Coutts, 1989). Angles that affect root anchorage include

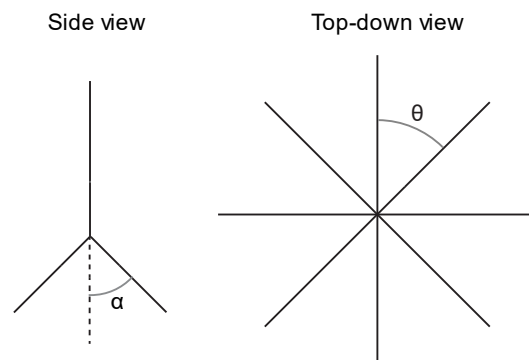


Figure 2.4: Branch angles  $\alpha$  and  $\theta$

the internal branching angle,  $\alpha$ , and the branch spacing angle,  $\theta$ , as shown in Figure 2.4.

The internal branching angle is defined as the angle between the main vertical axis through the taproot to the central axis of a root. This angle is referred to in forestry-based literature as the liminal angle for first order laterals.

A variety of other architectural parameters have notable relations to root anchorage. These parameters include root depth, root diameter, root length, root material properties, and more. The additional parameters mentioned are either well-defined in engineering at large (e.g. material stiffness) or have a variety of interpretations (e.g. depth from the surface versus depth to a point of dichotomy). For this reason, the additional parameters will be defined on an as-needed basis.

### **2.3 VERTICAL PULLOUT CAPACITY**

Along with nutrient uptake, root systems provide stability and anchorage for plants under forces such as wind loads, uprooting by herbivores, canopy weight, and soil displacement on slopes (Hamza, Bengough, Bransby, Davies, & Hallett, 2004). Root anchorage capacity has largely been studied to assess how roots affect and improve slope stability. While the loading types mentioned are often multi-directional, many roots and root models have been tested under unidirectional, vertical loading to measure the anchorage capacity of roots.

#### **2.3.1 Force distribution and failure mechanisms**

Forces applied to a plant distribute along the plant's reinforcing members and through to the roots. The anchorage capacity of the plant is mobilized when the forces in the roots transfer to the soil in the form of interface shear and bearing capacity (Ennos, 1989).

Hamza et al. (2004) tested the mechanical behavior of real roots and rubber root analogues to examine the soil-root interface behavior during vertical loading. Particle Image Velocimetry (PIV) was used to estimate soil strains and root deformation in pullout tests. The real roots were allowed to grow into the soil medium, while the rubber roots were halved longitudinally and placed against a clear surface. The observed response of the roots tested was a gradual spread of force down the length of the root as the test was carried out. Initially, the roots increased in length while the root tips stayed in place. The peak strength of the root system typically occurred when root tip displacement was initiated, which was then followed by one of three failure mechanisms. The failure mechanisms are explained in Table 2.1.

**Table 2.1:** Failure mechanisms observed by (Hamza, Bengough, Bransby, Davies, & Hallett, 2004) and hypothesized causes of failure

<b>Failure mechanism</b>	<b>Hypothesized cause of failure</b>	<b>Location of Failure</b>
Pullout of the entire root system	Low soil-root interface strength, causing the formation of thin shearing bands along the soil-root interface	Soil-root interface
Breakage of the root near the main stem	Smaller root cross-sectional area (i.e. higher concentrations of stress within the root)	Root material
Breakage within the root system in combination with soil bulb extraction	Low soil strength (potentially causing deformation of cracks)	Soil medium

For recorded pullout displacements of less than 4mm, there was negligible difference in the pullout response of the root analogues with varying number and arrangement of laterals. This suggested that roots deeper than 4 millimeters did not yet affect the pullout response because the pullout load had not distributed to the laterals.

Displacement greater than 4 millimeters showed large differences in the axial force necessary to pull branched versus unbranched roots from the ground. The laterals contributed to

increasing pullout resistance. There were two models with laterals, one with one set of laterals and the other with two sets of laterals, one deeper than the other. For the models with laterals, there is minimal difference in pullout resistance until about 20mm head displacement. This suggests that the root-analogue deformation is not occurring deep enough to engage support from the deep laterals of the second model. The model with two laterals shows greater pullout capacity than all the others at displacements greater than 20mm. The distribution of load through the root system allows for the mobilization of shear strength and will depend on the material properties of the root.

### **2.3.2 Root material**

The defining material properties that affect the load distribution are root material stiffness, soil stiffness, and root-soil interface strength (Mickovski, Bransby, Bengough, Davies, & Hallett, 2010).

#### **2.3.2.1 Root stiffness**

Mickovski et al. (2007) performed a comparative analysis on the root pullout behavior of model roots and real roots in both wet and dry sand and with varied material properties. The model roots were made of o-ring rubber and linden wood dowels, where the modulus of elasticity was on average 29 MPa and 1264 MPa, respectively. Three basic root systems were modeled including a singular taproot, a herringbone pattern root system with two lateral elements, and a dichotomous root system with two lateral elements. Similar to Hamza et al. (2004), some of the model roots were halved and placed against Perspex viewing faces to observe root-soil interactions during testing using PIV.

The results of the tests, as shown in Figure 2.5, show that the wooden roots had a 2x-4x greater maximum pullout resistance than the rubber roots except in the case of a singular

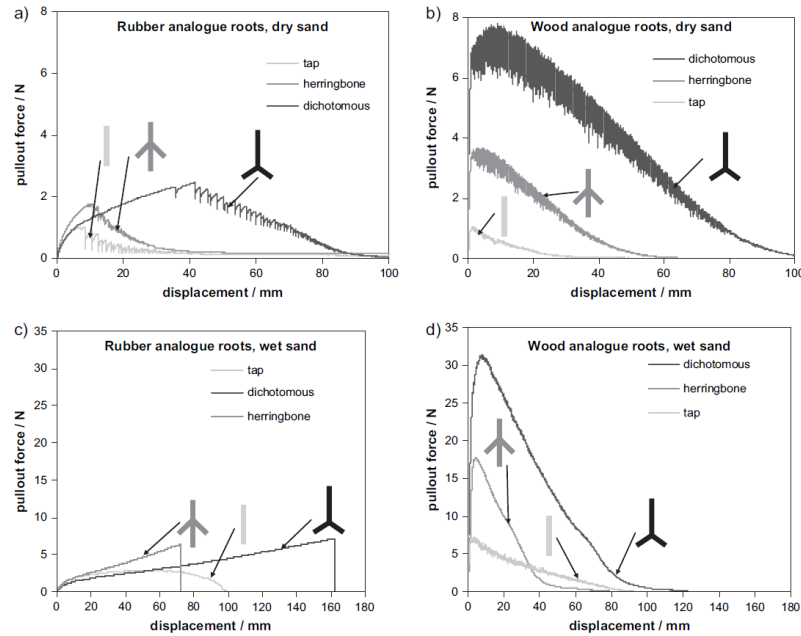


Figure 2.5: Load versus displacement curve for analogue (Mickovski, Benough, Bransby, Davis, & Hallett, 2007)

taproot in dry sand, for which the resistance was similar. The wooden root tests reached maximum pullout resistance at lower vertical displacements than the rubber roots.

This was reasoned to be a result of the relatively instantaneous mobilization of root-soil interface strength for the wooden roots because of the rapid load transfer to the soil. In comparison, the rubber model had a more gradual mobilization of interface shear strength from the top to the bottom of the root system. The rubber's lower stiffness allowed laterals to bend into the path of least resistance. Once there, the roots could be pulled out axially rather than laterally uplifting against a soil face. There was a difference in root diameter resulting in a 29% greater root surface area for the wooden roots relative to the rubber roots, but Mickovski et al. (2007) does not suggest that this is the main reason for the pullout resistance differentiation.

### 2.3.2.2 Root-soil stiffness ratio

Model roots made from the same wood and rubber materials as in Mickovski et al. (2007)

were used in Mickovski et al. (2010) to further explore the effect of root stiffness on root anchorage behavior, particularly with respect to the root-soil stiffness ratio. The model roots were designed as a singular taproot to simplify the effects of architecture on the pullout behavior. The soil stiffness was not estimated but was regarded as much lower than that of the wooden model roots. In this frame of reference, the rubber roots are regarded as flexible roots, particularly so in saturated sand versus dry sand.

During axial loading, the rubber roots stretched significantly and cause radial contraction, which reduced the interface shear stress. For flexible roots, pullout capacity is reduced with large enough axial strains in the material.

### 2.3.2.3 Root-soil interface friction angle

For the tests performed in Mickovski et al. (2010), the same model root materials were molded in a block form to perform direct shear tests to determine interface properties with the sand used for pullout testing. The peak and residual interface friction angles for the wood and rubber are shown in Figure 2.6.

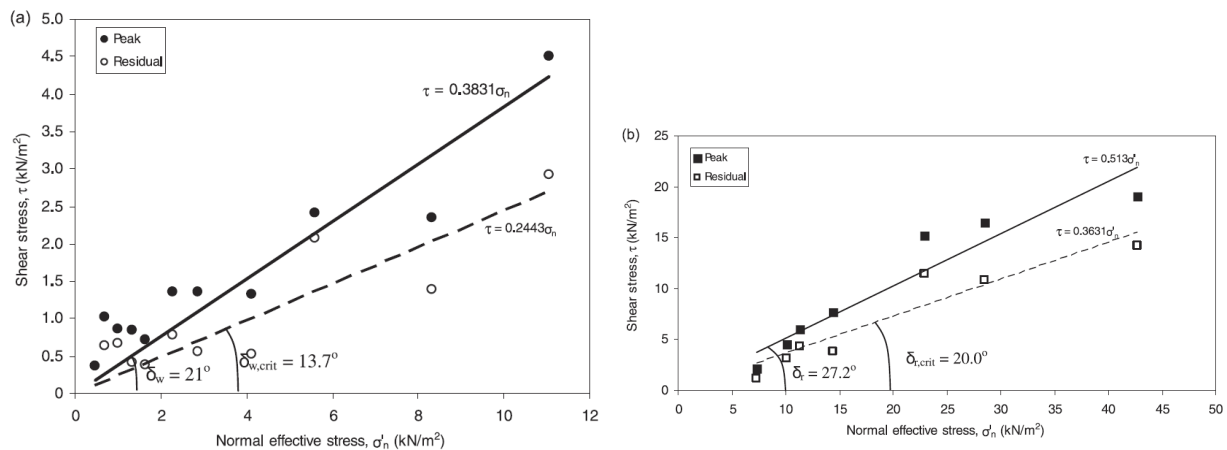


Figure 2.6: Interface shear test results for (a) wood-sand interface and (b) rubber-sand interface (Mickovski, Bransby, Bengough, Davies, & Hallett, 2010)

#### 2.3.2.4 Lateral earth pressure coefficient, $K$

The direct shear tests shown in Section 2.3.2.3 were used to understand the mobilized pullout forces using Equation 2.1 and 2.2. The variables are defined in Table 2.2.

$$F_{max} = \pi d \int_0^L K \sigma'_v(z) \tan \delta dz \quad 2.1$$

$$F_{max} = \pi d L K \overline{\sigma'_v} \tan \delta \quad 2.2$$

**Table 2.2:** Definition of variables for Equations 2.1 and 2.2

Variable	Description
$F_{max}$	Uplift capacity
$L$	Vertical root length
$d$	Constant root diameter
$K$	Lateral earth pressure coefficient
$\sigma'_v$	Vertical effective stress at depth $z$
$\overline{\sigma'_v}$	Average vertical effective stress adjacent to the root surface
$z$	Depth
$\delta$	Secant interface friction angle

Equations 2.1 and 2.2 assume that peak shear strength occurs across the root simultaneously, and that there is a singular interface friction angle. Effective stress is assumed to vary linearly with depth. Using the interface friction angles from the direct shear tests, the variable  $K$  was altered to fit Equation 2.2 to the pullout force versus root length data. For wood with a diameter of 2.3 mm,  $K = 5.12$ . For rubber with a diameter of 8.6 mm,  $K = 2.55$ .  $K$  differed greatly between the two materials. Different diameters of wood were tested to see how diameter affected  $K$ , and Mickovski concluded that  $K$  decreases with increasing diameter and is not significantly affected by material type (Mickovski, Bransby, Bengough, Davies, & Hallett, 2010).

### 2.3.3 Root architecture

Root architecture is comprised of the root quantity, volume of roots, topology of roots, and root dimensions.

#### 2.3.3.1 Root quantity and volume

Ennos (1990) studied the pullout capacity of leek seedlings to assess a predictive model for the pullout behavior. The results of the study showed strong similarity between the predictive model and the test results. Correlations between root length and pullout capacity indicated that many thin roots extending away from the main stem would provide more material efficient anchorage than one central taproot extending downward.

Mallett (2019) tested model root analogues with one set of laterals at the base of a main stem but differing number of laterals placed equidistantly from one another. The pullout tests using these root analogues indicated that the most material efficient (i.e. unit of capacity per unit of material volume) number of laterals was three.

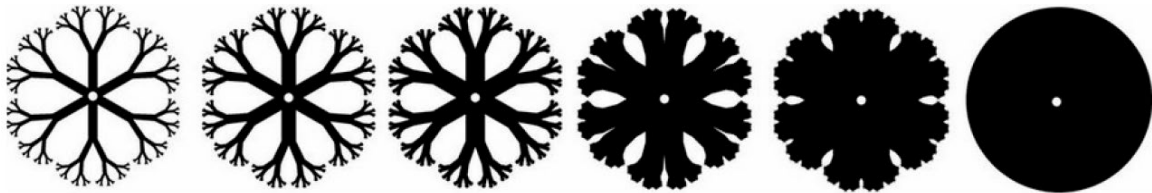


*Figure 2.7: Fractal plate designs for model anchors (Dyson & Rognon, 2014)*

An experiment was performed to estimate the efficiency of an anchor relative to the number of branching points formed by a fractal design (Dyson & Rognon, 2014). The models were all plate anchors, where the plate was a circular disc or variants of a fractal design with differing branch widths, as shown in Figure 2.7. Conclusion from tests showed that the plates with lower surface area had lower pullout resistance than those with higher surface area but that the pullout resistance of anchors with lower surface areas were more material

efficient (i.e. had a greater pullout resistance per material surface area) than those with higher surface areas.

#### 2.3.3.2 Dichotomous vs. herringbone topology

An investigation on the resistance of model root systems to uprooting was performed using artificial roots made of steel wire (Stokes, Ball, Fitter, Brain, & Coutts, 1996). Five root arrangements were used in testing. Three of the five (Type 1, Type 2, and Type 3) were used to create a model for predicting pullout force. The other two (Type 4 and Type 5) were used to test the model and compare herringbone versus random arrangement, where random is between dichotomous and herringbone structures. The arrangements of the five models are shown in Figure 2.8.

The computer model for predicting the uprooting forces of the model root pullout tests was based on the correlation of pullout force to cumulative vertical root depth, cumulative horizontal root span, and depth of the lateral roots. For Type 1, Type 2, and Type 3, the model aligned with all but one of the test models from Type 2 and was therefore believed as an accurate reference to predict the root pullout behavior for model roots with differing arrangements. Type 4 and Type 5 were tested and compared to the predictive model's pullout force to yield very similar results, with a highest standard deviation of 6.5% from the model. From the pullout resistance model and the testing results, the research indicates that a more dichotomous branching pattern will provide more anchorage than a herringbone pattern.

#### 2.3.3.3 Branch length and depth

A widely regarded conclusion in root anchorage research is that anchorage capacity increases with increasing root depth which coincides with increasing root length. Ennos

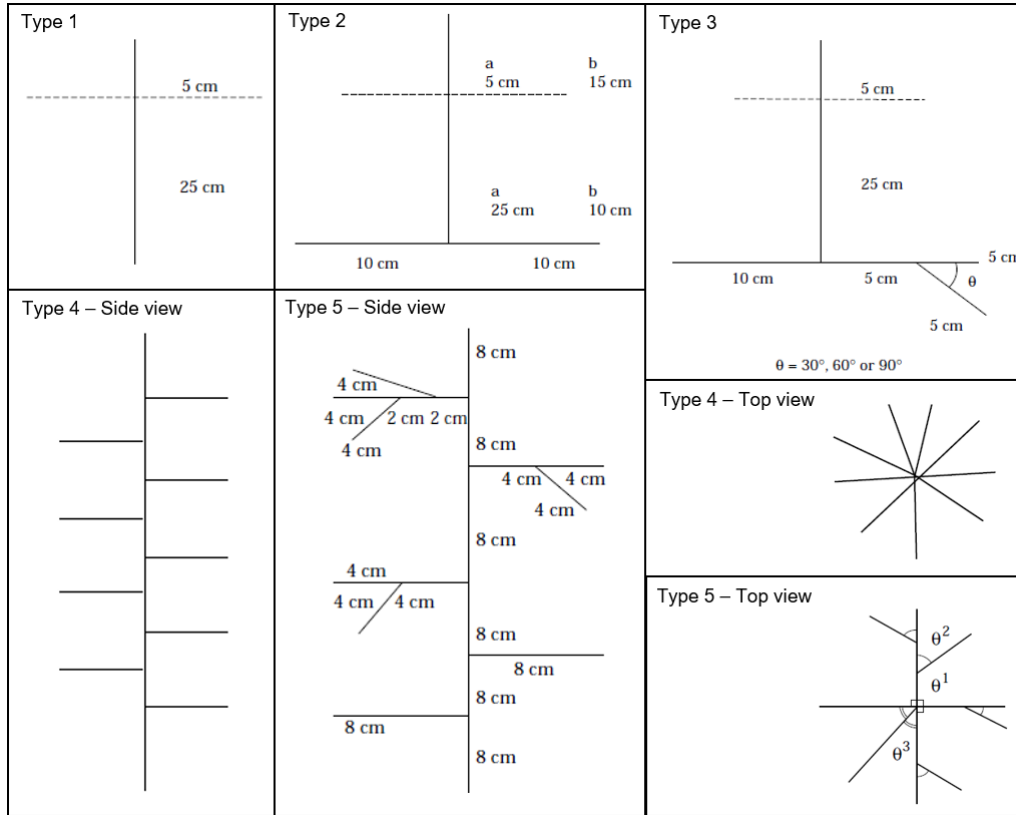


Figure 2.8: Schematic of all types of model roots tested in Stokes et al. (1996)

(1990) predicted and proved that pullout resistance rose with root length. A critical length was identified, which occurred at the depth for which the stresses in the branch surpassed the root material strength. The critical length was approximated using the Equation 2.3.

$$L_{crit} = \frac{\sigma R}{2\alpha\tau}, \quad 2.3$$

Equation 2.3 is derived assuming a perfectly vertical root with uniform cross-sectional area in a homogeneous, perfectly plastic soil body with infinitely high shear stiffness and a shear strength,  $\tau$ . The breaking stress for the root is represented as  $\sigma$ . The radius,  $R$ , accounts for the root cross-sectional area. The  $\alpha$  represents the root-soil bond as a value ranging from 0 (no bond) to 1 (bond as strong as the soil's shear strength). Root portions beyond the critical length will not contribute to anchorage capacity under this model. This concurs with the

understanding of tensile load distributing from the top to the bottom of the root, in which for some cases, the tensile load dissipates before reaching root ends.

The results of the model from Stokes et al. (1996) also indicated a significant reliance of anchorage on root depth. This reliance was attributed to increasing shear strength of the soil with depth. The herringbone branching arrangement was tested in pullout when the upper half branches were removed and when their lower half branches were removed to compare the effect of lateral root depth in relation to pullout resistance. Similarly, the random arrangement was tested when the second order laterals were in the top half of the root system and when in the bottom half of the root system. The latter set of tests was performed to compare the effect of depth of the second order laterals to pullout. For all tests, the models with more branches in the lower half yielded higher pullout resistance than those with branches in the upper half. The herringbone model had a 35% drop in pullout resistance with only upper laterals present versus lower laterals present. The random model had a 19% drop in pullout resistance when the second order laterals were present in the upper region versus the lower region. These results indicate that the amount and location of first order laterals was more critical to pullout capacity than the amount and location of second order laterals. The conclusions from testing support the positive correlation between root depth and pullout resistance.

Hamza et al. (2004) (see Section 2.3.1) concluded in pullout testing of rubber roots that the presence of a second set of laterals at greater depth increased the pullout resistance relative to a model with the same taproot length but only one set of laterals at a shallow depth.

Fibrous roots were tested in pullout and then measured for their cumulative root length (Mallett, 2019). When the cumulative root length was plotted against pullout capacity, a positive, linear correlation with an  $R^2$  value of 0.7331 was identified, showing the strongest relationship to pullout capacity of all the other factors measured in testing.

#### 2.3.3.4 Branch angles

The model from Stokes et al. (1996) discussed in Section 2.3.3.2 was used to predict optimal branching angle between the lateral and the main stem as well as the second order lateral relative to the first order lateral that it is connected to. The model suggests that a  $90^\circ$  angle between the first order lateral and the main stem is optimal to resist pullout. An angle between  $0^\circ$  and  $20^\circ$  was deemed ideal for the angle between the first and second order laterals. The latter prediction was interpreted to indicate the position at which second order laterals were held in tension rather than in torsion, which would occur for higher angles from the first order lateral.

These predictions were compared with the structure and behavior of real roots from a young European larch. The high variability in the real root system's arrangement yielded high amounts of scatter when plotted against model predictions. Despite this, the real root analysis agreed with the trend of near  $90^\circ$  lateral-to-main-stem angle and smaller angles between the first and second order laterals, though not as small as  $20^\circ$ , with an average of  $58^\circ \pm 13.6^\circ$ .

The work performed by Mallett (2019) tested a variety of internal branching angles for root analogues with a varying number of laterals extending from the base of the main stem. For models with three and six laterals, the optimal internal branching angle (see Figure 2.4 for definition) for maximizing pullout force was  $60^\circ$  and ranged as high as  $75^\circ$  depending on

the depth-to-width ratio of the root system. Mallett also notes that an internal branching angle less than  $90^\circ$  allows for effective use of overlying soil.

#### 2.3.3.5 Branch diameter

In Mickovski et al. (2010) and as described in Section 2.3.2.4, wooden model taproots of differing diameters were tested in “rigid” pullout tests. The resulting pullout forces increased with increasing diameter but had a nonlinear relationship, suggesting that the lateral earth pressure coefficient was not constant. The conclusion of this experiment suggests that a smaller diameter will have a larger cavity expansion ratio, causing larger increases in lateral earth pressure.

## 2.4 LATERAL AND MOMENT CAPACITY

The performance of tree roots under lateral and moment loading is applicable in many scenarios, such as a tree under wind load. The simplified force diagram of a tree under lateral loading are shown in Figure 2.9.

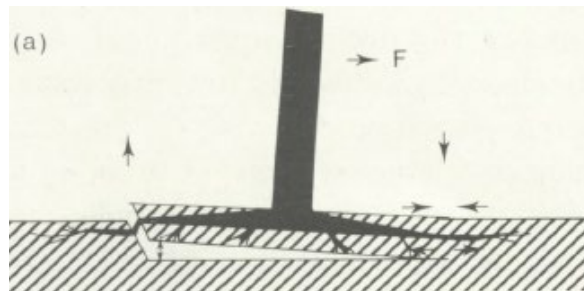


Figure 2.9: Force diagram on tree root system under lateral loading (Coutts, 1989)

### 2.4.1 Number and presence of laterals and sub-laterals

The presence of horizontal laterals extending perpendicular to the main stem is suggested to resist rotational movement in (Stokes, Ball, Fitter, Brain, & Coutts, 1996). The horizontal laterals resist tension which helps keep the taproot vertical. Under loading, the main laterals near the surface help strengthen the soil on the side that is uplifting (windward side). The main laterals on the compressed side (leeward side) bend, creating tension on one side of the root which helps reinforce the soil on the leeward side. If only a few primary laterals branch from the main stem, the failure of the tree will likely result because of a stiff root system. Too many

branches causes the fulcrum of the lateral moving stem to be near the surface and therefore less stable (Coutts, Root architecture and tree stability, 1983).

### 2.4.2 Combined loading

Vertical, horizontal, and moment loads can act in conjunction in tree root systems under wind and gravity loads. The behavior of structures subjected to multi-directional loads has been explored using finite element modeling (Gourvenec, 2007). Using a circular surface foundation

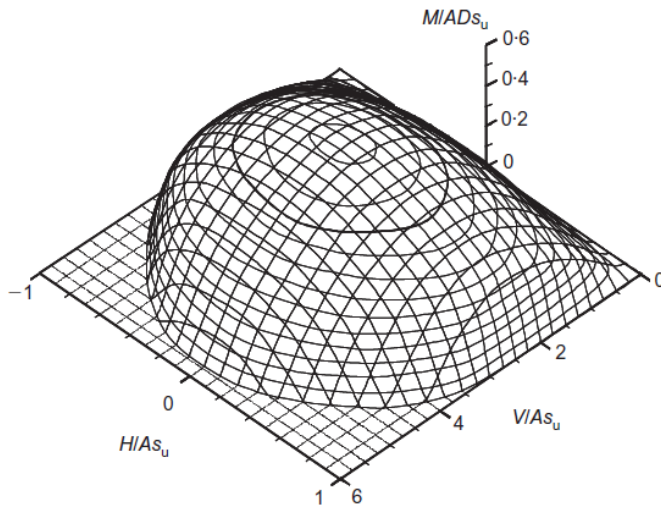


Figure 2.10: Multi-directional failure envelope for circular plate foundation on uniform soil with no bonding at the foundation-soil interface (Gourvenec, 2007)

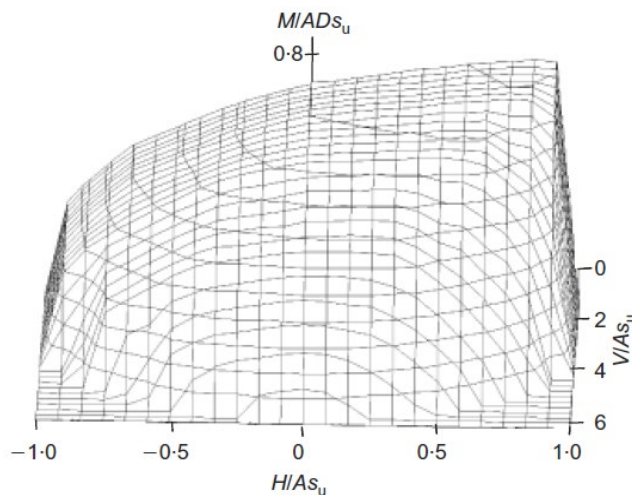


Figure 2.11: Multi-directional failure envelope for circular plate foundation on uniform soil with no bonding at the foundation-soil interface (Gourvenec, 2007)

and zero-tension foundation-soil interface, a failure envelope was estimated for combinations of directional loading. The resulting failure envelope is shown in Figure 2.10.

The results suggest that there is a peak capacity under a combination of positive

horizontal load and moment.

Alternatively, a finite element model was performed where the circular foundation was bonded at the foundation-soil interface. The resulting

failure plane is shown in Figure 2.11.

This updated failure plane suggests that there is asymmetry dependent on the directions of the moment and horizontal loads.

## CHAPTER 3     ULTIMAKER S5: BUILDING A MODEL

### 3.1   EQUIPMENT INFORMATION

The Ultimaker S5 is a dual extrusion, Fusion Deposition Modeling (FDM) 3D printer. The printer can be used to create 1-material or 2-material 3D models. With the 2-material feature, the printer can create a model with water-soluble supports. The water-soluble supports allow for the construction of intricate models wherein traditional supports cannot be removed or leave a rough texture when removed. The 3D printer is useful for printing arbitrary shapes that would otherwise be difficult to form with materials like metal or wood.

### 3.2   SOFTWARE SET-UP

The Ultimaker S5's printing capabilities are dependent on the user's familiarity with 3D modeling software and the Ultimaker software, Ultimaker Cura.

#### 3.2.1   3D Modeling software

Models for the Ultimaker S5 can be created in most any 3D modeling program. For this work, the tree root models and relevant parts for testing were created in AutoCAD and Solidworks.

##### 3.2.1.1   AutoCAD

AutoCAD is useful for creating models using relative dimensions. The program is developed with the trigonometry-savvy user in mind. Embedded reference planes form as the user creates models. These reference planes help to connect multiple parts using reference points on the planes. Parts are not linked to one another unless specified, even if a part is created relative to another part's dimensions. This parts autonomy allows for flexibility in the process of creating a multi-faceted model. Though this may be subjective to the author's familiarity with the programs, it is suggested that AutoCAD is a user-friendly program that allows for mistakes without requiring the deletion of a large portion of the model. AutoCAD was used to create most of the model drafts.

### 3.2.1.2 Solidworks

Solidworks does not create planes of reference but rather forces the user to create planes of reference. This is an extra step that is not required of AutoCAD users.

Solidworks is advantageous for making holes using the Hole Wizard feature embedded in the program. In AutoCAD, a hole is created by cutting out a section of a model given dimensions defined by the user. Solidworks has a large variety of pre-defined hole sizes based on standardized screws/bolts/etc. This was particularly useful in creating 3D printed attachments to connect via screws to a robotic arm.

## 3.2.2 Ultimaker Cura

Ultimaker Cura is the 3D model program used to create support structures on a model and to format the model file to be interpreted by the printer. Once a 3D model is built, it can be imported to Cura as a variety of file types. For the tree root model testing, models were imported as '.stl' files.

### 3.2.2.1 Base settings

The printer has pre-defined settings for the first-

time user as shown in Figure 3.1. The internet and particularly Ultimaker's website have valuable guidelines for how to print a model using these predefined settings. The base setting to begin the tree root 3D printing process was the Default, 0.1 setting with 100% infill density. Some useful links for understanding the 3D printer are listed in Table 3.1.

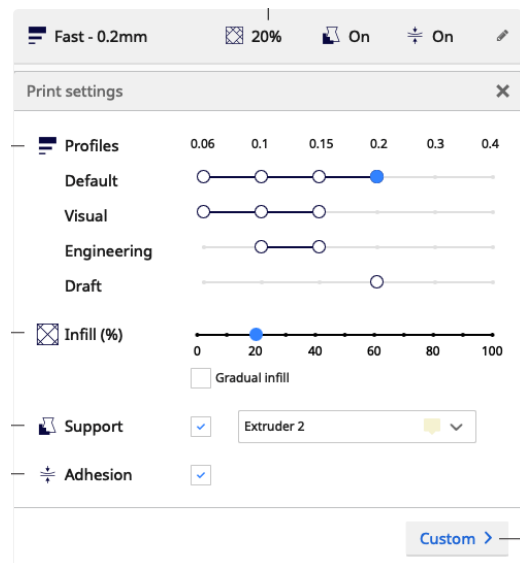


Figure 3.1: Ultimaker Cura base setting interface (support.ultimaker.com)

**Table 3.1:** Useful links for 3D printing

Content	URL
Overview of basics	<a href="https://support.ultimaker.com/hc/en-us/sections/360003504180-Ultimaker-S5">https://support.ultimaker.com/hc/en-us/sections/360003504180-Ultimaker-S5</a>
Print settings	<a href="https://support.ultimaker.com/hc/en-us/articles/360011432580-Prepare-a-print-for-the-Ultimaker-S5-with-Ultimaker-Cura">https://support.ultimaker.com/hc/en-us/articles/360011432580-Prepare-a-print-for-the-Ultimaker-S5-with-Ultimaker-Cura</a>
Start a print	<a href="https://support.ultimaker.com/hc/en-us/articles/360011432680-How-to-start-a-print-on-the-Ultimaker-S5">https://support.ultimaker.com/hc/en-us/articles/360011432680-How-to-start-a-print-on-the-Ultimaker-S5</a>
Remove a print	<a href="https://support.ultimaker.com/hc/en-us/articles/360011432940-Remove-the-print-from-the-Ultimaker-S5">https://support.ultimaker.com/hc/en-us/articles/360011432940-Remove-the-print-from-the-Ultimaker-S5</a>
Infill density	<a href="https://support.ultimaker.com/hc/en-us/articles/360012607079-Infill-settings">https://support.ultimaker.com/hc/en-us/articles/360012607079-Infill-settings</a>
Material properties	<a href="https://core-electronics.com.au/tutorials/ultimaker-printing-material-comparison.html">https://core-electronics.com.au/tutorials/ultimaker-printing-material-comparison.html</a>

### 3.2.2.2 Settings for tree root models

The tree root models proved a particular challenge to print. To attain similar surface roughness between models, the initial goal was to print the models standing upright in the printer. Their slender, tall frames and small sizes were difficult to support and print in an upright manner. The Ultimaker Cura settings to achieve a successful print were adjusted after the base settings were applied and are described in Table 3.2.

Ultimately, the models had to be printed laying flat rather than standing upright, as shown in Figure 3.2. This is because the settings could not be fine-tuned enough to print the models



upright without total failure or *Figure 3.2: Successful model print layout*

significant stringing. Considerations made before resorting to laying flat are listed in Table

3.2. Additionally, a third-party add-on was used which allows the user to create support structures where they want. Support structures were created to surround the long, narrow section of the model. However, this strategy was ultimately not used for printing of the anchor models.

### **3.3 MATERIAL SELECTION**

Every project will have specific criteria for the material properties of the 3D printed models. A variety of materials were tested for use in the tree root model testing program.

#### **3.3.1 Commonly used materials and their properties**

The materials listed are all Ultimaker brand. A list of advantages and disadvantages for each material is displayed in Table 3.3.

##### **3.3.1.1 Accuracy of print dimensions**

When printing with a variety of these materials, it became evident that the materials were not printing exactly to the dimensions specified in the model save file. To test this, a model cube was printed with precise dimensions and measured after printing with three materials, ABS, PC, and Tough PLA. The ABS printed most to dimension, followed by the PC, and lastly Tough PLA. Comparisons to other materials on the list were not made but should be investigated if dimensionally accuracy is necessary for testing.

#### **3.3.2 Support materials**

The two support materials, Breakaway (Thermoplastic polyurethane Polylactic acid) and PVA, are used for different purposes. When printing a model, the model material must be extruded at a particular temperature. The higher the printing temperature of the filament, the less likely it will be possible to successfully print with PVA since this material prints at a low temperature. Breakaway can withstand higher

**Table 3.2:** Settings to print clean print in Ultimaker S5

Print setting	Tree root setting	Reason for change
Infill pattern	Cubic	Cubic is strong under 3D loading.
Retraction distance	7 mm	Retraction should be enabled. Adjusting the retraction distance helps to prevent filament stringing between parts of the model.
Retraction speed	30 mm/s	Helps to prevent stringing
Maximum retraction count	25	Helps to prevent stringing
Print speed	40 mm/s	Prevents under-extrusion of filament
Z-hop when retracted	Enable	Prevents print nozzle from bumping into parts of the print
Support placement	Everywhere	Places supports anywhere they are needed
Overhang angle	60°	Determines how Cura decides what features of the model need supports
Support pattern	Triangle	Creates stable supporting structure
Support density	20%	Sets the infill density of the supports to be enough to support the model and easily removed from the model
Enable conical supports	Enable	Helps with material use efficiency and reduces print time
Minimum layer time	20 sec	Allows a given layer to cool before the next layer is placed
Minimum speed	10 mm/s	Provides a base level speed that the nozzle heads cannot move slower than
Enable prime blob	Enable	Primes the nozzle before print begins
Build plate adhesion type	Brim or raft	Helps prevent warping of the model and helps removal of the model
Prime Tower	Size=15mm	Helps prime nozzles during transition from one material type to another

temperatures. If PVA is printed with a material like ABS, which has a very high printing temperature, the adhesion between the two materials will be poor since the ABS will likely burn the PVA. Therefore, the two material combinations considered were ABS with breakaway supports and tough PLA with PVA.

**Table 3.3:** Ultimaker material advantages and disadvantages (core-electronics.com/au)

<i>Material</i>	<b>Advantages</b>	<b>Disadvantages</b>	<b>Soluble in</b>
<i>PLA</i>	Prints high resolution with glossy finish	Can be brittle as the print ages	NaOH
<i>Tough PLA</i>	Less brittle than PLA, tougher than PLA, matte finish	--	NaOH
<i>ABS</i>	Tough and durable	Prone to warping, has high printing temperature	Acetone
<i>Nylon</i>	High durability, high strength, flexible, high abrasion and corrosion resistance	Cannot withstand hot temperatures for long	--
<i>CPE</i>	Tough, dimensionally stable, chemically resistant	--	--
<i>CPE+</i>	Higher impact resistance and temperature resistance than CPE	--	--
<i>PC</i>	Retains dimensional stability under 110°C, good for molds, tools, and functional prototyping, strong, tough	--	--
<i>TPU 95A</i>	Qualities similar to flexible rubber	Doesn't perform well in UV exposure, moist environments, or high temperatures	--
<i>PP</i>	High strength to weight ratio, smooth surface finish, good temperature, electrical, and chemical resistance	--	--
<i>PVA</i>	Good support structure material	Weak, humidity sensitive	Water
<i>Breakaway</i>	Good for support structure, low moisture absorption rate	--	--

### 3.3.3 Tree root model material combination

Initially, the goal was to print the tree root models using Ultimaker ABS and Ultimaker Breakaway supports. ABS is a strong material that prints best to dimension of the materials tested. When the models were printed with Breakaway supports, the Breakaway would not break away without applying a force that snapped the ABS models or left Breakaway material on the model. ABS and Breakaway was not suitable for printing tree roots. The final combination of materials was Tough PLA with Natural PVA water soluble material as supports. Tough PLA had a similar strength to ABS, was less brittle than ABS, and did not require breakaway support material.

### 3.4 PRINTING PROCEDURE

The steps taken before and after a print can improve the quality of the print and can prevent breakage of the print during or after removal.

#### 3.4.1 Pre-print procedure

There are many steps to take before printing a model. After one or two filament materials have been selected and the Ultimaker Cura file aligns with those filament choices, the physical preparation can begin.

##### 3.4.1.1 Load filament spools

After gathering the appropriate spools for the project, Table 3.4. details the procedure for loading the spools. A variation to this method will be necessary when using materials that are sensitive to humidity. This variation is described in Section 3.5.1.1.

##### 3.4.1.2 Prepare glass plate

Steps to ensure the print adheres well to the glass plate are as follows:

1. Ensure that the glass plate is clean by using a lens microfiber cloth to wipe the glass.
2. Apply glue to glass surface and spread evenly with a damp microfiber sponge.
  - a. A thicker layer of glue should be used with Tough PLA and ABS materials.
  - b. If you know where the model will print on the glass, you can place glue only on that area rather than across the entire glass plate.
3. Place the glass surface into the printer and secure with metal clips.
4. (Optional) The Ultimaker S5 automatically calibrates the plate surface to be at the correct distance from the nozzle head. If a print is not adhering well to the surface, one consideration is to manually calibrate the nozzle head.

**Table 3.4:** Procedure to load filament spools

<b>Spool #2: Loading instructions</b>
<ol style="list-style-type: none"> <li>1. Under the “Configuration overview” tab, click the Load Material Wizard for Input #2.</li> <li>2. Loosen the free end of the filament</li> <li>3. Face the spool with the filament type label facing the printer</li> <li>4. Push the spool onto the spool hanger. When pulling the filament, the spool should rotate clockwise.</li> <li>5. For Ultimaker brand filaments, all of the material settings should automatically be recognized by the printer. For filament made by other manufacturers, the material properties must be defined at this point on the touchpad in the front of the printer.</li> <li>6. Once the material properties have been input, continue following the instructions on the 3D printer touchpad.</li> <li>7. Take the free end of the filament and push it through the bottom of the 3D printer intake for filament #2 (or if loading Spool #1, use intake box #1). The filament should be visible in the Bowden tube. If necessary, lift the clamp on the side of the intake box, push the filament in, and close the clamp. Click “Confirm” on the touchpad.</li> <li>8. The printer should now pull the material to the print head and begin extruding the material. When the material cleanly runs out of the print head, click “Confirm” on the touchpad.</li> </ol>
<b>Spool #1: Loading instructions</b>
<ol style="list-style-type: none"> <li>1. Under the “Configuration overview” tab, click the Load Material Wizard for Input #1.</li> <li>2. Loosen the free end of the filament</li> <li>3. Face the spool with the filament type label facing away from the printer</li> <li>4. Attach the tangle guard to the spool by pressing the attachment through the center of the spool.</li> <li>5. String the free end of the filament through the hole in the tangle guard.</li> <li>6. Push the spool on the printer and lock the guard onto the spool hanger.</li> <li>7. Ensure that when the filament is pulled, the spool rotates counterclockwise.</li> <li>8. Repeat steps 5 through 8 from Spool #2 instructions.</li> </ol>

#### 3.4.1.3 Upload print to printer

The print file can be loaded to the printer via USB. With the file on a USB drive, plug that USB drive directly into the printer. On the touchpad, the option to load a project from USB will appear. Click this option and select the file to be printed. The Ultimaker S5 will

automatically begin the printing process. The print takes 10-15 minutes to begin because of the calibration process mentioned in the Section 3.4.1.2.

### **3.4.2 Post-print procedure**

After printing, measures must be taken to ensure that the 3D model and the printer parts are not damaged and that the printer is set-up for the next print.

#### **3.4.2.1 Remove print from glass plate**

The model can be safely removed from the glass plate using a plastic or metal putty spatula and another object, such as a rubber mallet, to hit the handle of the spatula. A metal putty spatula poses a higher risk of damaging the print or scratching the glass plate. This risk is lessened using a raft or rim on the model.

When the print is complete, the glass plate will be hot. Safely remove the plate and set it down on a flat, clean surface. Use a small container to pour water on the base of the model. The purpose of doing this is to create a rapid cooling of the plate surface so that the model contracts and breaks its adhesion to the surface. This will not always fully remove the model.

If the model is still adhered to the plate, line up a spatula as near to parallel with the glass plate and with the end pressing lightly into the model or along the model raft. Use a rubber mallet or other tool to tap the end of the spatula repeatedly until it loosens the model from the plate.

#### **3.4.2.2 Remove structural supports from model**

*If using PVA for the supports:* Clip away as much of the supports as possible. After the supports have been clipped, soak the 3D print in water for 12-24 hours. The PVA will dissolve quicker if the water is kept moving around the sample.

*If using breakaway or PLA for the supports:* Clip the supports off as close to the surface of the print as possible. Smoothing the surface can be achieved by sanding the remaining ridges away or using a solvent, such as acetone (this depends on the material used for the supports).

#### 3.4.2.3 Perform nozzle cleaning (hot pull and cold pull)

The nozzles can get caked with burnt filament during the printing process. To prevent build-up, it is recommended to routinely perform one nozzle cleaning procedure after every print. The procedure for cleaning the nozzle is detailed in the program on the touch pad of the printer. The program can be found in *Preferences* → *Maintenance* → *Print head* → *Print core cleaning*.

After selecting which core to clean, use PLA filament to continue the procedure (unless Ultimaker cleaning filament is available). The program will automatically remove filament from the print head just enough to remove the Bowden tube. After removing the Bowden tube, follow the on-screen instructions to perform a hot pull then cold pull.

Additionally, the outside of the nozzle can be cleaned by raising the temperature of the nozzle head and using tweezers to remove melted filament. To raise the temperature of the nozzle head, go to the configuration menu and select the nozzle to be cleaned. In the top right corner, the three-dot icon can be selected to show the option to set the print head temperature. The nozzle head should be brought to 150°C for cleaning purposes. Too hot and the filament will burn.

### **3.5 COMMON ISSUES**

Even with the most assured of set-ups, prints can fail. Some common reasons include humidity, low filament extrusion, and incorrect Cura settings.

### 3.5.1 Humidity

Some of the materials are especially sensitive to humidity exposure. These materials include Ultimaker Natural PVA, Ultimaker TPU95A, Ultimaker PC, and Ultimaker Nylon. If the filament has absorbed too much moisture, the print may fail. A crackling sound and bubbling filament indicate evidence of over-exposure to moisture as seen in Figure 3.3. The filament may also feel soft and sticky to the touch. If this is to occur, the filament



*Figure 3.3: Ultimaker PVA, damaged by humidity*

should be dried per Ultimaker support's recommendations. A cautionary mention that filament can also be too dry. An indicator of an overly dry spool of material is that the material will crack easily and, in the case of Natural PVA, have an opaquer sheen. If this occurs, the spool of material is bad and should be disposed of.

#### 3.5.1.1 Polymaker Polybox II

A more permanent solution to ensure that this does not occur is to place the filament spools in a sealed container with desiccant packs during the printing process to keep the humidity between 10 and 20 percent. The Polymaker Polybox II is designed to perform this purpose, having small openings for the filament to travel through while protecting the filament. Since the filament inside the Polybox will have a longer travel path to the print nozzle, there will be greater friction on the filament as it travels. This can cause grinding of the filament at the feeder on the back of the Ultimaker S5. If grinding occurs, the feeder box should be opened and cleaned with compressed air and a small brush.

Minimizing friction along the filament path will prevent grinding. This is done by placing the Polybox in a location where the natural curvature of the filament follows the curvature of the Bowden tubes. Though not tested with the equipment for this research, the ideal

arrangement of Polybox relative to the Ultimaker is to have the Polybox below the 3D printer. If this cannot be done, experiment with different Polybox locations until grinding does not occur. Another means of reducing friction is to remove the provided Bowden tubes that connect from the Polybox to the back of the printer. This will cause some exposure of the material to external humidity, but not enough to damage the filament beyond use. There is also a grippy hole cover on the Polybox that can be removed for further friction reduction. The final means of reducing friction is to raise the filament spools off the metal tracks in the Polybox. A 3D model of a spool holder can be printed for this purpose, as shown in Figure 3.4.



Figure 3.4: 3D-printed filament spool holder  
(Source: <https://www.thingiverse.com/thing:4307246>)

#### 3.5.1.2 Storage

Aside from using the Polybox as humidity protection, all filament spools should be stored in a sealed container with desiccant packs. This will help to preserve the longevity of the spools. Prompt removal of the spools from the printer after a print is done will ensure that exposure to the room's humidity will have the least time to affect the spool material quality.

#### 3.5.2 **Low filament extrusion**

Low filament extrusion can be a separate issue from humidity levels. In the case of printing for this research, low filament extrusion was linked to humidity levels. When a filament has too much water in it, the filament can start to burn inside of the print nozzle. The filament can also burn if the nozzle is set at too high a temperature, if the material is grinding in the feeder, and if the material is sitting in the hot nozzle for an extended idle period.

Every scenario has a different preventative measure. Ensuring that the filament is not overly moist will prevent humidity effects. Ultimaker materials have a recommended nozzle temperature range that should be adhered to. Material grinding in the feeder can be a result of a variety of issues, but one easy way to alter the strength of the feeder grip is to loosen the grip hold with Ultimaker’s provided hex driver. Leaving a model print on pause for too long can cause the filament burning. Though not arranged for the equipment used in this research, a camera monitoring the print will allow the user to notice if the print has paused. If the print can be un-paused or stopped entirely, the filament will be less likely to burn in the nozzle.

### 3.6 FINAL PRINTED PARTS

The parts printed successfully and used in this research are shown in Figure 3.5.

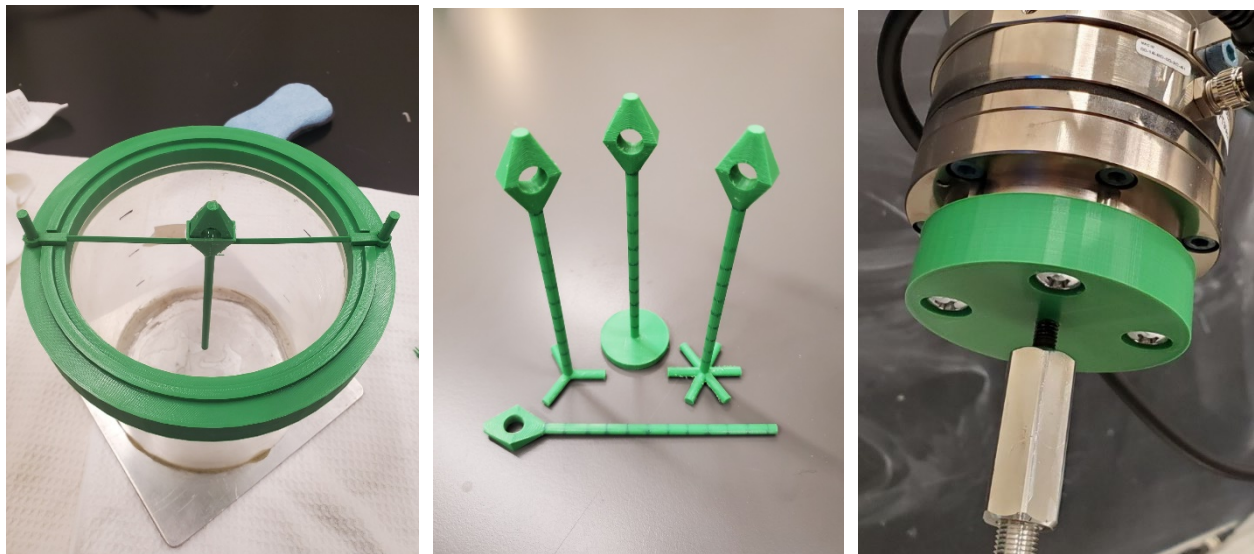


*Figure 3.5: From left to right: Model holder for use during sand pluviation, the four selected models for testing, and the tool connector used to attach the model to the robotic arm*

The plate and pile model were printed as reference anchors to see if the tests performed as expected and to see how the non-traditional tree root designs compared. The 3-leg and 6-leg tree root model were selected to explore whether these arrangements would result in improvements in anchor efficiency, which is measured in terms of unit capacity per unit volume of anchor ( $N/m^3$ ). The tree

root models have an internal branching angle of 90° (see Figure 2.4). The dimensions of the models are detailed in Table 3.5.

**Table 3.5:** Model dimensions

<b>Model</b>	<b>Model Part</b>	<b>Dimension (mm)</b>
All	Stem length	110 (105 below sand surface)
Plate	Plate end diameter	40
Plate	Plate end thickness	5
6-leg, 3-leg	Overall diameter of branch extent	40
6-leg, 3-leg	Branch diameter	5

## CHAPTER 4 UNIVERSAL ROBOTS UR16E

### 4.1 EQUIPMENT INFORMATION

The Universal Robots UR16e is a collaborative six-axis robotic arm with a 16kg payload. The arm has an embedded six-axis force and torque sensor in the tool end. The robotic arm's functionality ranges from assembly line worker to research tool. For this research, the embedded force and torque sensor were not adequate to get high resolution data at low force and torque values (sub 10 N, sub 0.05 N-m respectively). To resolve this issue, the 6-axis F/T Sensor: Axia80-M20 was attached to the UR16e tool end, recording at 0.1 N force resolution and 0.005 N-m torque resolution. Relevant parts of the robotic arm are shown in Figure 4.1. Given the fact that robotic arms have only been employed in a limited number of geotechnical studies i.e. (Jin, Shin, & Hambleton, 2020), the goal of this chapter is to provide background information regarding the

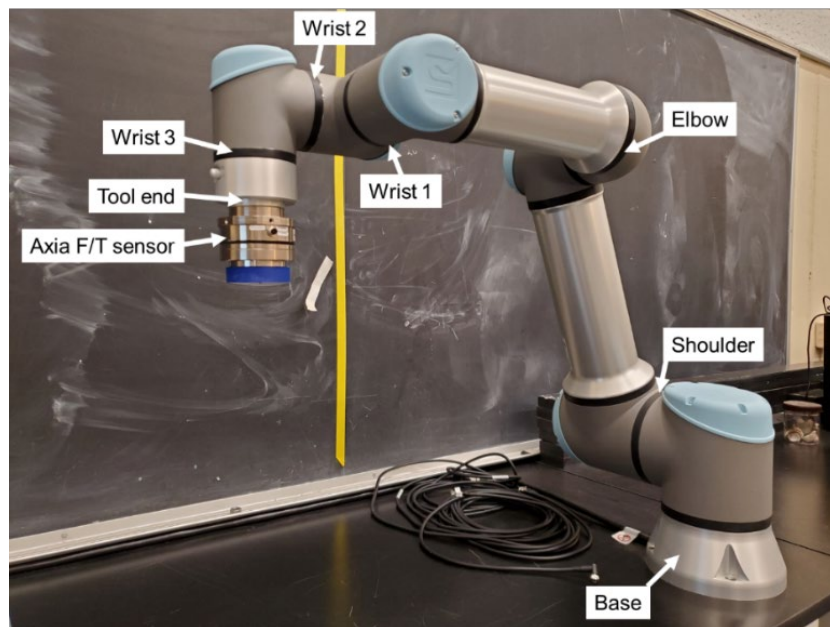


Figure 4.1: Robotic arm parts diagram (not pictured are the control box and the Teaching Pendant)

robotic arm's use, configuration, and control, and the post-processing of the data obtained from the 6-axis F/T sensor.

## **4.2 TEACHING PENDANT: USING POLYSCOPE**

The UR16e robotic arm is equipped with a tablet called the Teaching Pendant. The Teaching Pendant runs a program called Polyscope that is used to write basic movement programs for the arm. There are numerous useful Polyscope user guides provided online by Universal Robots. The steps taken to move the robotic arm for the purpose of the research are particular and extend beyond the scope of what the online guides teach.

### **4.2.1 Password Protections**

The UR16e has multiple protective measures to ensure that the robot is being used safely and within the scope that the user defines.

#### **4.2.1.1 Manual vs. Automatic**

The robotic arm has two modes of functioning: manual and automatic. Automatic mode is built to allow the robot to function at maximum efficiency without allowing anyone to change the program or robot installation settings. Manual mode is password protected and allows the user to change the program that is running, to move the robot using the 'Move' tab in Polyscope, and to edit the robot installation settings.

When first setting up the robot, it is necessary to set a password\* for Manual mode. To set this password, the following steps must be taken.

1. Go to 'Settings' in the menu tab in the top right of the screen.
2. Click on the 'Password' tab on the left of the screen.
3. If a password has never been set, input 'easybot' for the Current password.

4. Create a new password in the ‘New password’ prompt.
5. Confirm new password by rewriting the password in the next prompt.
6. Apply to confirm the password change.

\*Current password: gmlsoils

#### 4.2.1.2 Safety Password

The safety configurations can be defined by the user after setting a safety password\*. To set a safety password, the following steps must be taken.

1. Go to ‘Settings’ in the top right menu tab.
2. Select ‘Password’ on the left panel, then select ‘Safety’.
3. In the ‘New password’ tab, type a password
4. Confirm the password by re-writing in the next line.
5. Apply the changes.

\*Current password: MischiefManaged

#### **4.2.2 Tool Configuration**

The Axia F/T sensor changes the load on the robotic arm’s tool. The tool center point (TCP), center of gravity, and payload must be assessed to allow the robotic arm to function safely and accurately. Polyscope has wizard programs built to estimate all of these values. The wizards are valuable; however, it is important to understand what the wizard is calculating in the case that these values must be calculated manually.

#### 4.2.2.1 Tool Center Point

The TCP is located at the center of connection between the tool and parts that the tool holds (e.g. the pin and the 3D printed model). To use the TCP wizard, the TCP tab in Installation → General should be selected. The ‘Measure’ wizard on the right of the position coordinates can be selected to trigger a guided series of maneuvers to estimate the tool position. The orientation wizard on the same tab can be used if a tool is off-center from the load cell.

#### 4.2.2.2 Center of Gravity and Payload

Similar to the TCP, a built-in wizard guides the user through the process of identifying the center of gravity and the payload. Under the Payload tab in Installation → General, a ‘Measure’ wizard can be selected to start this process. Knowing the mass of the end attachment is beneficial since the wizard is not always accurate. Manual input of the mass of the end attachment is possible in the Payload tab.

### **4.2.3 Writing a program**

Writing a program in Polyscope is a similar experience to writing a code in MATLAB or Python, except that Polyscope has simplified the process of calling commands. To start a program in Polyscope, click on the Program tab on the top left of the Polyscope screen. For the following explanation, only the critical variables and commands under the basic tab are discussed.

#### 4.2.3.1 Moving the robotic arm

The robot can be moved using the arrows in the Move tab on the left-hand side of the screen. The arrows move relative to the selected feature. If the base selected is the feature

drop-down menu, the arrows move the robot in reference to the coordinate system of the base. If the TCP is selected, the arrows move the robot in reference to the tool coordinate system. The coordinates of both the base (blue dot) and the tool (red dot) are shown in Figure 4.2. When a given feature is set, for example the tool, all movements of the tool will be relative to the red dot.

The robot can also be moved manually by holding one hand down on the ‘Freedrive’ button and using the other hand to manually move the robot. This is easier with two people, where one holds the ‘Freedrive’ button and the other uses two hands to move the robot. The ‘Freedrive’ settings allow restriction of movement or rotation along or about the x-, y-, and z-coordinates of the base of the robot.

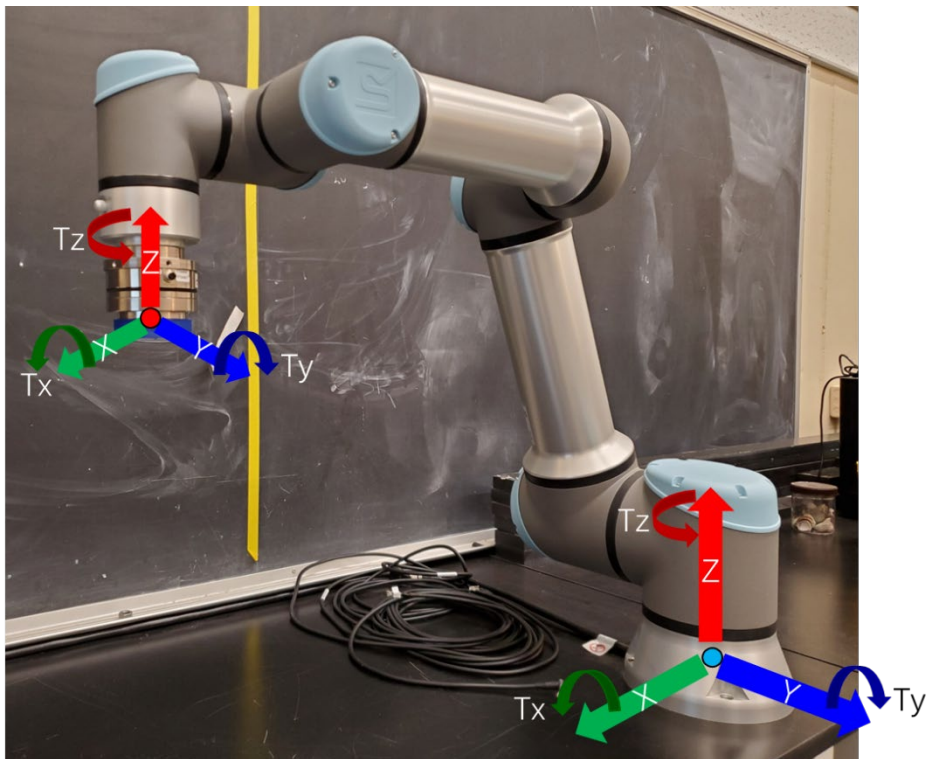


Figure 4.2: Coordinate systems of the tool (red dot) and the base (blue dot)

#### *4.2.3.1.1 Feature coordinates*

Feature coordinates can be used to move an object relative to the feature's coordinate system. The robot has two built in features, the base and the TCP, which is defined as stated in Section 4.2.2.1. If the robot is to be moved relative to the TCP, then the TCP location will always be the origin of the reference coordinate system. If the tool moves, the coordinate system moves. This specific feature is useful when the start point of a program is the location of the TCP (or user defined feature) and the endpoint of the program is always relative to the start point.

Since the TCP feature is already defined, the steps left are to define the waypoint relative to the feature. In the Move command settings, a drop-down menu titled 'Feature' will contain all defined features. The TCP should be selected. After this is selected, all points will be defined relative to the TCP.

#### *4.2.3.1.2 Angled movement of TCP*

When setting angled positions of the TCP, the feature can be base or TCP. On the right-hand side of the screen, Rx, Ry, and Rz for the TCP will be shown. These are the rotation measurements along the x-, y-, and z-plane of the specified feature. Any value in the direction pane can be selected after which another screen will pop up. The value of Rx, Ry, and Rz can be changed to angle the tool at a specific angle relative to the feature coordinates.

#### 4.2.3.2 Variables and commands

A few critical variables and commands when using Polyscope are 'Waypoint', 'Move', 'Wait', and 'Halt'. A capture of an already written program with some of these commands

and variables can be found in Figure 4.3.

#### *4.2.3.2.1 'Waypoint' variable*

A waypoint is defined as a location of the TCP set by the user. When the waypoint variable is added to the program by clicking Program → Basic → Waypoint, the waypoint can be defined by clicking the 'Set point' button and moving the robot to a waypoint using the functions in the Move tab.

#### *4.2.3.2.2 'Move' command*

There are three possible ways that the arm can move in a program including 'MoveJ', 'MoveL', and 'MoveP'. All commands involve defining waypoints along the robot's path.

'MoveJ' is used when the path from one point to the next does not matter. The robot will select the path most efficient for speed of the robot's movement, typically moving in a nonlinear path from one point to another.

'MoveL' moves from one point to the next in a linear path. The speed and acceleration of movement along the path can be defined for 'MoveL'.

'MoveP' is the same as 'MoveL' except that 'MoveP' does not pass directly through intermediate waypoints. Instead, the 'MoveP' command asks the user to define a blend radius that defines the circular path the robot will take inside intermediate points. The purpose of rounding direction changes of the TCP is to allow a constant speed when passing through waypoints.

#### 4.2.3.2.3 'Wait' command

The wait command can be used to pause the program between two commands. The time of the pause can be defined within the command parameters.

#### 4.2.3.2.4 'Halt' command

The halt command can be placed at the end of the program to stop the program from rerunning. Without the halt command, the program will cycle until the program is manually stopped on the teaching pendant.

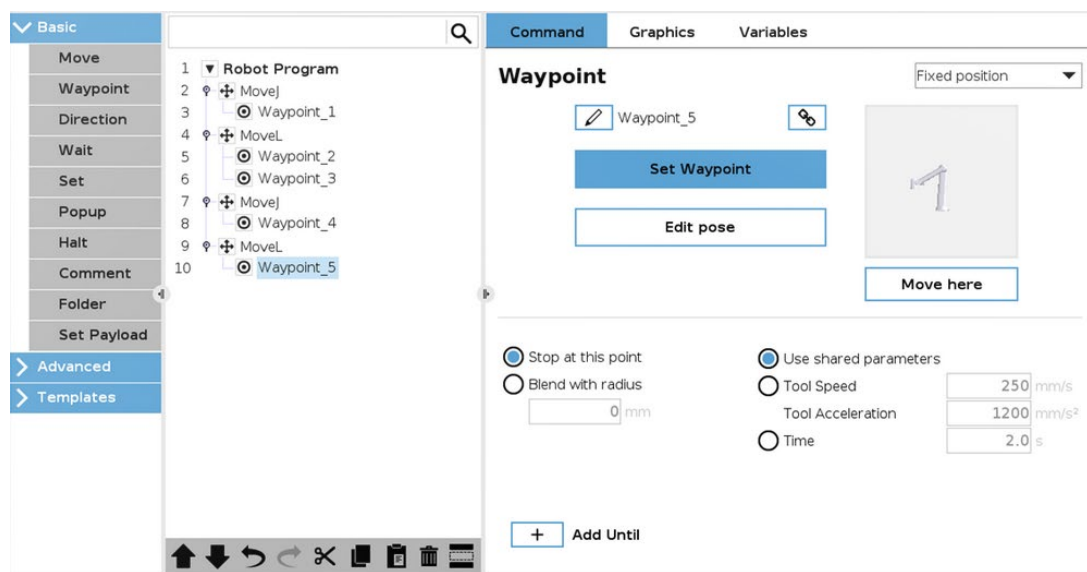


Figure 4.3: Example program written to move the robot between five waypoints

### 4.3 COMMUNICATING WITH THE UR16E AND THE AXIA F/T SENSOR

The UR16e and the Axia F/T sensor each have unique requirements necessary to acquire data from their sensors.

#### 4.3.1 Ethernet Connection

The robotic arm and Axia F/T sensor were connected for data acquisition via ethernet cables. A 5-port ethernet switch connects all of the equipment to the local computer and connects the computer to internet. The arrangement of ethernet cables is shown in Figure 4.4.

### 4.3.2 Communication with UR16e

The UR16e is primarily controlled through Polyscope. Polyscope is meant to be user friendly. When trying to acquire more information from the robotic arm, such as force and torque values from the internal load cell, a more intricate approach must be taken.



Figure 4.4: Ethernet connection system for UR16e and Axia F/T sensor.

(Sources: <https://thinkbotsolutions.com> <https://www.nwca.com/> <https://www.lifewire.com/>)

#### 4.3.2.1 Defining an IP address for the UR16e

To define the IP address of the UR16e, select an unused IP address that matches the first nine digits of the desktop's IP address, with the last one to three digits being different from any other equipment on the network. For example, if the IP address of the computer is 123.456.789.100, then a potential IP address for UR16e is 123.456.789.101. The subnet IP address should be the same for both the desktop and the UR16e.

Once an IP address has been selected, power on the teaching pendant. In the Settings menu in the top right corner of the screen, go to the 'Network' tab. Within this tab, the IP address can be manually altered if static IP address is used. This is where to input the selected IP address of the UR16e.

#### 4.3.2.2 Obtaining Real-Time Data Exchange (RTDE)

The robotic arm can report real time data. A large variety of information can be obtained through RTDE, including the force and torque values of the internal load cell. The ultimate guide for RTDE can be found on the [UR website](#). On that website, there is a downloadable zip file including the necessary base code to obtain the RTDE. The code to record RTDE is in the example folder and is titled ‘record.py’. The coding language is Python. This code is run and controlled on a desktop that is linked with the robotic arm. The code does not have the power to move the robot, though there can be code written for this purpose.

In line 36 of the code, as shown in Figure 4.5, the default should equal the IP address of the desktop. The name of the host to connect to should be the IP address of the robotic arm.

The frequency of the data pull can be changed in line 39. The output file name can be

changed in line 41. The columns of data that are output can be changed in the ‘rtdc.py’ file.

The code will run when it is told to and will stop using the command ‘Ctrl+c’. The file will output where the user has designated it to.

```

34 #parameters
35 parser = argparse.ArgumentParser()
36 parser.add_argument('--host', default='localhost', help='name of host to connect to (localhost)')
37 parser.add_argument('--port', type=int, default=30004, help='port number (30004)')
38 parser.add_argument('--samples', type=int, default=0, help='number of samples to record')
39 parser.add_argument('--frequency', type=int, default=125, help='the sampling frequency in Herz')
40 parser.add_argument('--config', default='record_configuration.xml', help='data configuration file to use (record_configuration.xml)')
41 parser.add_argument('--output', default='robot_data.csv', help='data output file to write to (robot_data.csv)')
42 parser.add_argument("--verbose", help="increase output verbosity", action="store_true")
43 parser.add_argument("--buffered", help="Use buffered receive which doesn't skip data", action="store_true")
44 parser.add_argument("--binary", help="save the data in binary format", action="store_true")
45 args = parser.parse_args()

```

Figure 4.5: Lines of code in the RTDE “record.py” file that are relevant for connecting to the robot

### 4.3.3 Communication with Axia F/T Sensor

The Axia F/T sensor is a non-UR associated device that was built for UR robotic arms. The sensor connects to the robot’s control box for power and to the desktop for communication via ethernet.

#### 4.3.3.1 Powering the Axia F/T sensor

The Axia F/T sensor is powered by the robot's control box. Five free wires extend from the Axia F/T sensor. The brown wire is the positive voltage (V+), and the brown/white wire is the negative voltage (V-). The other three wires are not necessary for powering the F/T sensor and should be covered with electrical tape. The V+ and V- wire should be

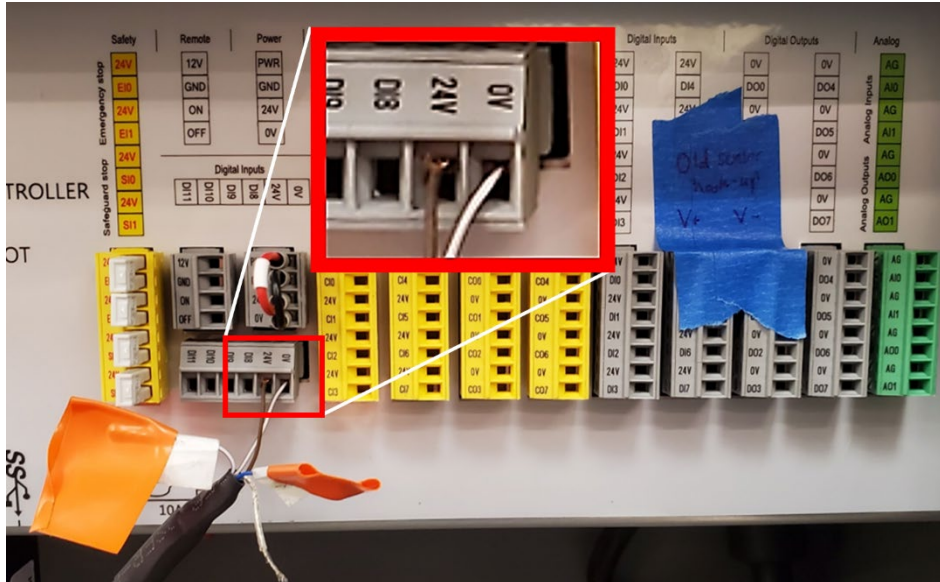


Figure 4.6: Control board cable arrangement to power the Axia F/T sensor

inserted into respective 24V and 0V on the control board inside the control box of the robot as shown in Figure 4.6.

#### 4.3.3.2 Using the Axia F/T sensor program

In the Axia F/T sensor manual, there is an extensive description for how to configure the sensor to communicate with the desktop and associated programs (accessible at [https://www.ati-ia.com/app\\_content/documents/9610-05-Ethernet%20Axia.pdf](https://www.ati-ia.com/app_content/documents/9610-05-Ethernet%20Axia.pdf)). The Axia F/T sensor needs an IP address similar to the UR16e but with differing end digits. For

example, if the robotic arm's IP address is 123.456.789.101, then an appropriate IP address for the Axia F/T sensor is 123.456.789.102.

There is a Java® demo program that must be downloaded once connection has been made with the Axia F/T sensor. This program will require the IP address of the F/T sensor to access the webpage with configurations for the load cell. The sampling frequency can be edited on this webpage. Once the IP address has been input and connection has been established, the demo program allows the user to pull real time data. The 'Bias' button zeroes the F/T readings. The data can be recorded using the log data feature in the top left corner of the program.

#### 4.4 ROBOTIC ARM TESTING ALIGNMENT

The anchor load tests were performed on 3D printed models attached to an assembly of parts, as shown in Figure 4.7. The connection between the model and arm is a pinned connection that does not carry moment, with the pin located at the top of the model. The model is free to rotate about the X-axis while the robotic arm and other parts move along the Z-axis.

##### 4.4.1 Robotic arm position

Seven angles were selected for testing, 0° (vertical), 15°, 30°, 45°, 60°, 75°, and 90° (horizontal). The robotic arm was programmed to align to each of these angles using 'MoveL'.

Waypoints were defined at the initial connection

point of the model and at a point along the angled path where the model is breaking the surface.

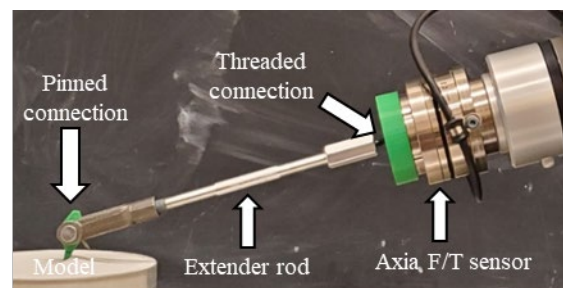


Figure 4.7: Assembly of parts used to connect the robotic arm to the model

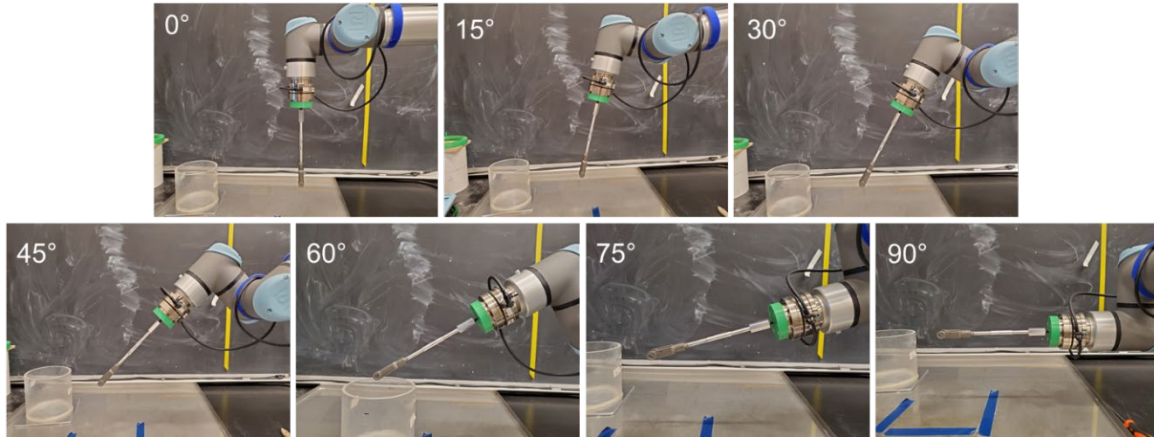


Figure 4.8: Robotic arm test alignment

The varying angles are shown in Figure 4.8. Each of the four root models, as described in Chapter 3, were tested at  $0^\circ$ ,  $15^\circ$ ,  $30^\circ$ ,  $45^\circ$ ,  $60^\circ$ ,  $75^\circ$ , and  $90^\circ$ . The Axia F/T sensor was aligned in one direction for tests  $0^\circ$ -  $60^\circ$  and was aligned in the opposite direction for tests  $75^\circ$ -  $90^\circ$ .

The directionality that comes with this difference in alignment is shown in Figure 4.9.

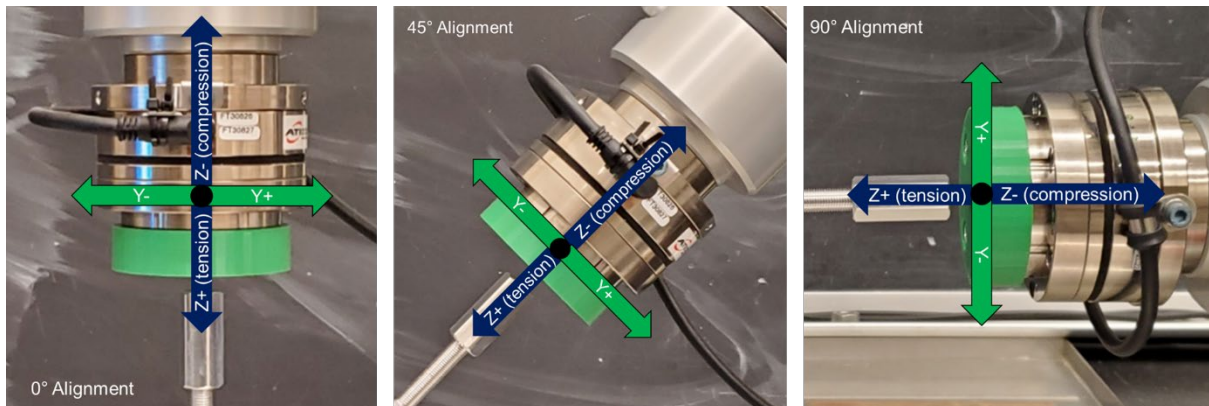


Figure 4.9: Directionality of load cell data relative to test alignment

## 4.5 DATA POST-PROCESSING

After performing tests, the data must be processed to display relevant, accurate values.

### 4.5.1 Zeroing the data

Though the experiment can be zeroed using the built-in function “bias” in the Axia software, zeroing the data manually is still necessary. At first, under the vertical test condition ( $0^\circ$ ), the

data was zeroed based on the end values of the experiment. This was done because, at the end of each experiment, the model was left free hanging to assess the weight of the model.

After performing this method at  $0^\circ$ , it became apparent that the effects of model weight could not accurately be measured for angles that approached horizontal. Because of this, the final form of zeroing the data was to subtract all values by the initial value in the data set to account for the weight of the model and the sand above it.

#### **4.5.2 Identifying the cutoff displacement**

For every testing angle, the displacement that the model underwent varied. At the lowest, only around 60 mm of data was attained. Because of the desire to compare data between angles, the data was cut off at 60 mm. Care was taken to ensure that critical values (i.e. the peak force) were not removed in the process of hiding all data recorded after 60 mm displacement.

#### **4.5.3 Calculating horizontal and vertical force data**

The sensor was not always aligned so that vertical was in the z-direction and horizontal was in the y-direction. Equations based on trigonometry were written to calculate the horizontal and vertical forces. The diagrams and equations used to complete this conversion are in Table 4.1.

Because the alignment of the Axia F/T sensor was varied between the tests at  $0^\circ$ - $60^\circ$  and  $75^\circ$ - $90^\circ$ , multi-level 'if' statements were used to convert the data using the formulas in Table 4.1.

After the horizontal and vertical forces are calculated, the resultant force is calculated using the Pythagorean Theorem.

**Table 4.1:** Discretization of data into vertical and horizontal direction.

0°-60° Alignment		75°-90° Alignment	
If...	Then...	If...	Then...
Z= (+)	$V =  z \cos\theta +  y \sin\theta$	Z= (+)	$V =  z \cos\theta -  y \sin\theta$
Y= (+)	$H =  z \sin\theta -  y \cos\theta$	Y= (+)	$H =  z \sin\theta +  y \cos\theta$
Z= (+)	$V =  z \cos\theta -  y \sin\theta$	Z= (+)	$V =  z \cos\theta +  y \sin\theta$
Y= (-)	$H =  z \sin\theta +  y \cos\theta$	Y= (-)	$H =  z \sin\theta -  y \cos\theta$
Z= (-)	$V = - z \cos\theta +  y \sin\theta$	Z= (-)	$V = - z \cos\theta -  y \sin\theta$
Y= (+)	$H = - z \sin\theta -  y \cos\theta$	Y= (+)	$H = - z \sin\theta +  y \cos\theta$
Z= (-)	$V = - z \cos\theta -  y \sin\theta$	Z= (-)	$V = - z \cos\theta +  y \sin\theta$
Y= (-)	$H = - z \sin\theta +  y \cos\theta$	Y= (-)	$H = - z \sin\theta -  y \cos\theta$

#### 4.5.4 Data filtration

A moving average was applied to reduce the noise in the data. 40 points were included in the moving average,  $\pm 20$  points from the point of concern. This equated to 2 mm of points included in the average value. To illustrate this filtering process, unfiltered versus filtered data is shown in Figure 4.10 for the plate model at 45° pullout.

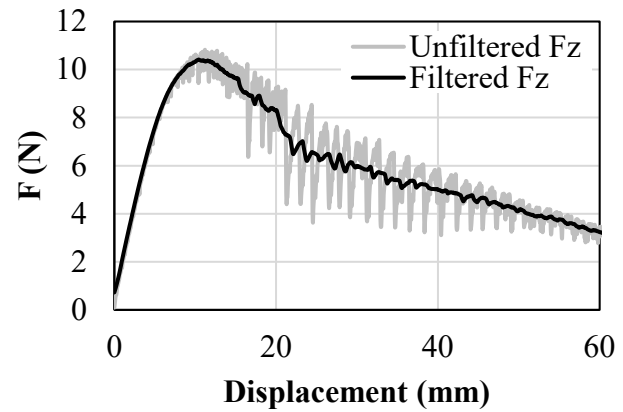


Figure 4.10: Unfiltered vs. filtered load vs. displacement data

## CHAPTER 5 RESULTS AND ANALYSIS

### 5.1 VERTICAL AND HORIZONTAL LOADING

The Axia F/T sensor on the tool end of the robotic arm is aligned at whatever angle the model is pulled at, as described in Chapter 4 and shown in Figure 4.8. The sensor returns a force in the x-, y-, and z-direction of the sensor coordinate system ( $F_x$ ,  $F_y$ , and  $F_z$ ). In Section 4.4.1, the z- and y-direction are identified as the predominant loading directions for the test. From these two directions, the forces in the vertical and horizontal direction were calculated (see Section 4.5.3). Section 4.5.3 of Chapter 4, along with Table 4.1, provide a description of the relationship and calculation of vertical and horizontal forces from  $F_x$ ,  $F_y$ , and  $F_z$ .

#### 5.1.1 Materials and methods

The materials and methods used in testing are described in the following sub-sections. Details on the 3D-printed models and their embedment depth are in Section 3.6.

##### 5.1.1.1 Soil Medium

Ottawa F-65 was used for the testing because of its availability and common use in laboratory studies. Ottawa F-65 is a silica sand. The particles are rounded to sub-rounded. The soil is poorly graded. The properties as reported by Palumbo (2018) of Ottawa F-65 are in Table 5.1.

**Table 5.1:** Properties of Ottawa F-65 (*Palumbo, 2018*)

	$G_s$	$D_{50}$	$e_{max}$	$e_{min}$	$C_u$	$C_c$	$\phi_{pk}(\text{°})$	$\phi_{res}(\text{°})$	$\psi(\text{°})$
Ottawa F-65	2.65	0.20	0.83	0.51	1.61	0.96	33.8	29.6	7.5

### 5.1.1.2 Pluviation

Ottawa F-65 was pluviated in a cylindrical container approximately 5.5 inches in diameter and in depth. The pluviator used is shown in Figure 5.1. Inside of the pluviator is a 3-hole system where the holes can be adjusted in size, as shown in Figure 5.1. The sand was pluviated in three lifts with approximately equal height to achieve an average relative density of 38% with a standard

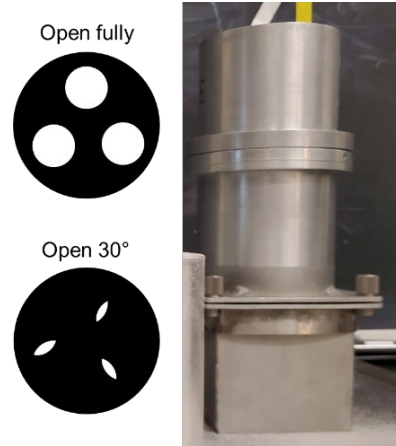


Figure 5.1: Pluviator used in testing

deviation of 2% and a maximum range from 33% to 43%. Each lift of sand was pluviated from a height of 6 inches from the soil surface to the base of the pluviator. A loose soil arrangement was selected to reduce the dilative tendency of the soil, since the tests were going to be performed at low confining pressure.

### 5.1.1.3 Robot program

The Axia F/T sensor recorded the force data versus time. The rate of movement was observed to be constant throughout the test, so displacement was linearly correlated to 0.05 mm every half second according to the rate of 0.1mm/s assigned in the test program. The details of the angles for the robotic arm positioning are described in Section 4.4.1.

## 5.1.2 **Load versus displacement curves for anchor load tests**

The results from each of the four models are presented in terms of force versus displacement. The forces shown are the measured Fz force in the direction of the displacement and the calculated vertical force and horizontal forces (see Section 4.5.3). For angles 0° and 90°, tests were performed 2 to 3 times to ascertain the repeatability of the tests. For all the repeated tests,

it was found that the results varied according to the measured relative density of the sample. Those tests which exhibited higher forces had higher relative densities.

#### 5.1.2.1 Pile

The force versus displacement data is shown for the pile model pulled out at all 7 angles in Figure 5.2. At 0° (vertical) the forces are imperceptible for the entire test, due to the small forces which are indistinguishable from the noise in the load cell sensor. Moving from 15° up to 90°, the Fz, V, and H magnitudes increase as the angle is increased. In addition, the peak of the force gradually starts occurring at greater displacements. This agrees with pile behavior, as the load transfer occurs primarily through skin friction at 0° and transitions to primarily through bearing capacity as the angle increases to 90° (Fleming, Weltman, Randolph, & Elson, 2008). As shown, the peak becomes less sharp as the angle increases. The load transitions from being larger in the vertical direction at 0° to larger in the horizontal direction at 90°. The Fz load typically matches or exceeds the higher load.

#### 5.1.2.2 Plate

The force versus displacement data for the plate model pulled out at 6 of the 7 angles is shown in Figure 5.3. It is noted that the results from the 30° test were inaccurate and were removed from the results analysis. As shown, the Fz, V and H force magnitudes are considerably larger than for the pile anchor. Like the pile data, the peak of the force transitions from early peak to later peak as the angle moves from 0° to 90°. The peak also becomes less sharp as the angle increases. The Fz matches the higher load force for 0°, 15°, and 90°. For all other angles, Fz lies between the vertical and horizontal loads.

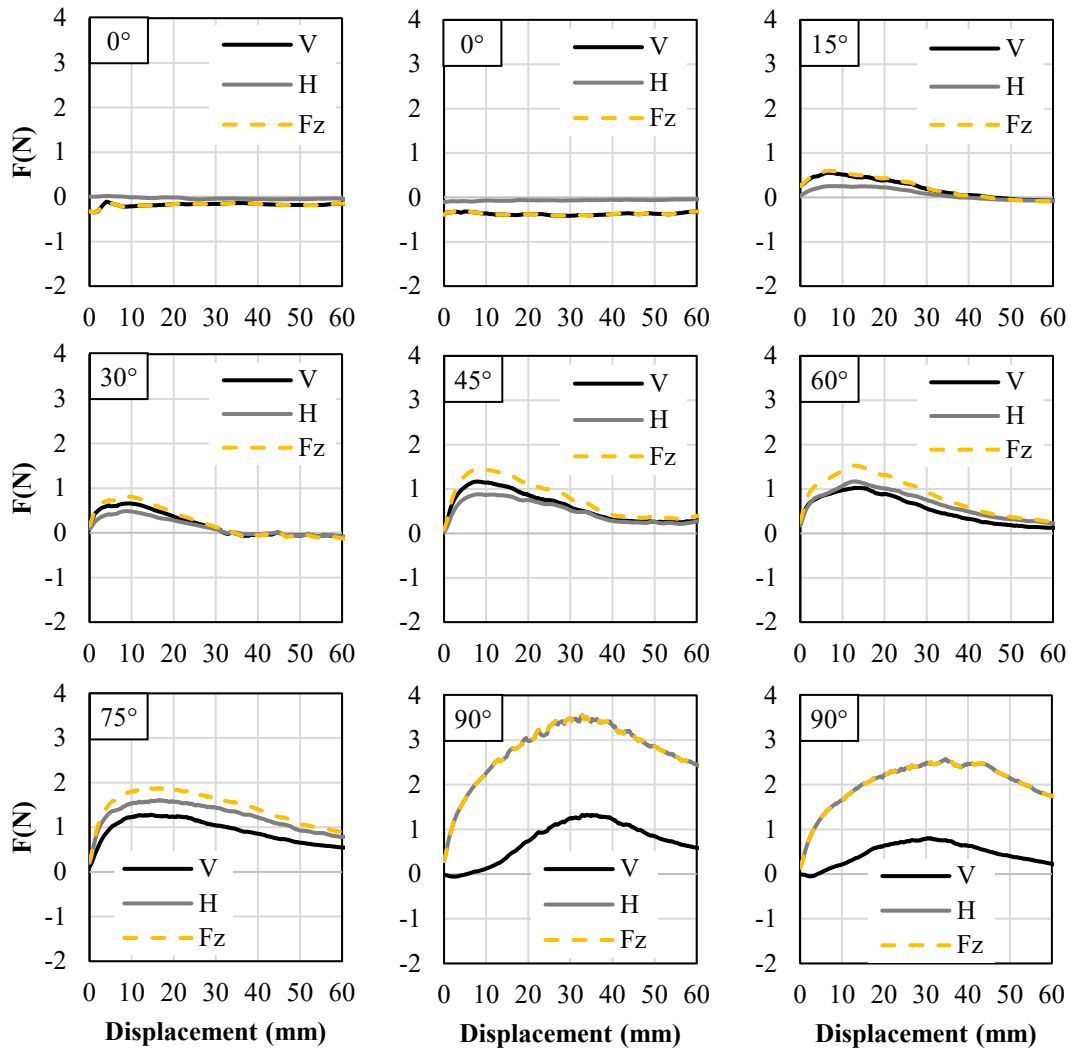


Figure 5.2: Force versus displacement for the pile model showing force in the vertical-, horizontal-, and z-direction

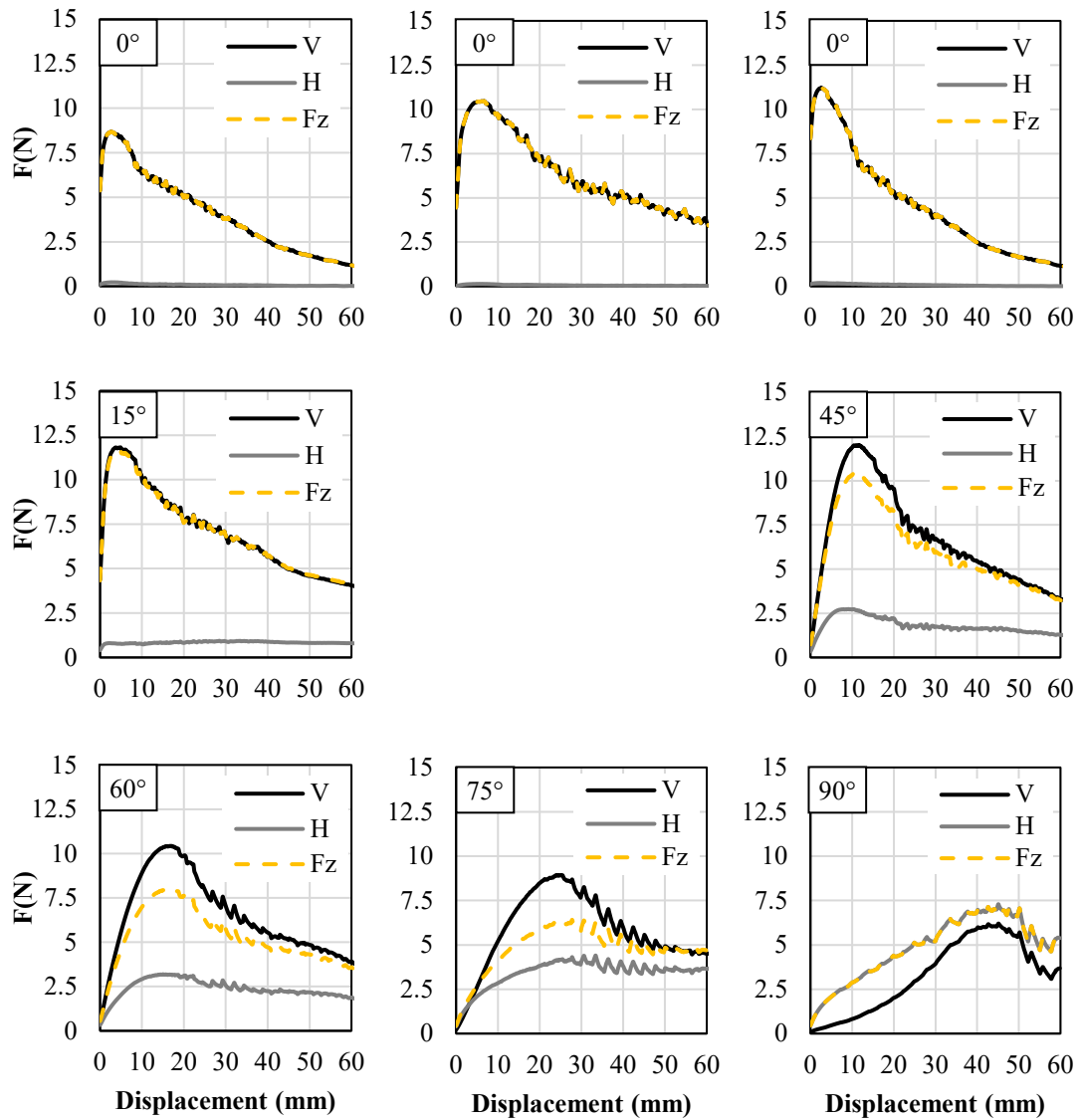


Figure 5.3: Force versus displacement for the plate model showing force in the vertical-, horizontal-, and z-direction

#### 5.1.2.3 6-leg

The force versus displacement data for the 6-leg model pulled out at all 7 angles is shown in Figure 5.4. The Fz, V and H force magnitudes are greater than those for the pile anchor but smaller than for the plate anchor. Like the plate model, the peak load transitions from an early peak to a later peak as the angle goes from 0° to 90°. The peak becomes less sharp as the angle increases from 0° to 90°. The greater load for 0° to 60° is the vertical load. The horizontal load is greater for 75° and 90°. The Fz closely follows the vertical load from 0° to 60°. For 75°, Fz is between the vertical and horizontal load magnitudes. Fz closely follows the horizontal load for 90°. The transition from carrying in the vertical direction to in the horizontal direction is because of the transition from load transfer occurring primarily through skin friction at 0° to primarily through bearing capacity as the angle increases to 90° (Fleming, Weltman, Randolph, & Elson, 2008).

#### 5.1.2.4 3-leg

The force versus displacement data for the 3-leg model pulled out at all 7 angles is shown in Figure 5.5. All the force magnitudes are smaller than for the 6-leg anchors but greater than for the pile anchor. Like the plate and 6-leg models, the peak load transitions from an early peak to a later peak as the angle goes from 0° to 90°. The peak becomes less sharp as the angle increases from 0° to 90°. The higher load for 0° to 60° is the vertical load. The horizontal load is higher for 90°. The Fz closely follows the vertical load from 0° to 75°. The Fz closely follows the horizontal load for 90°.

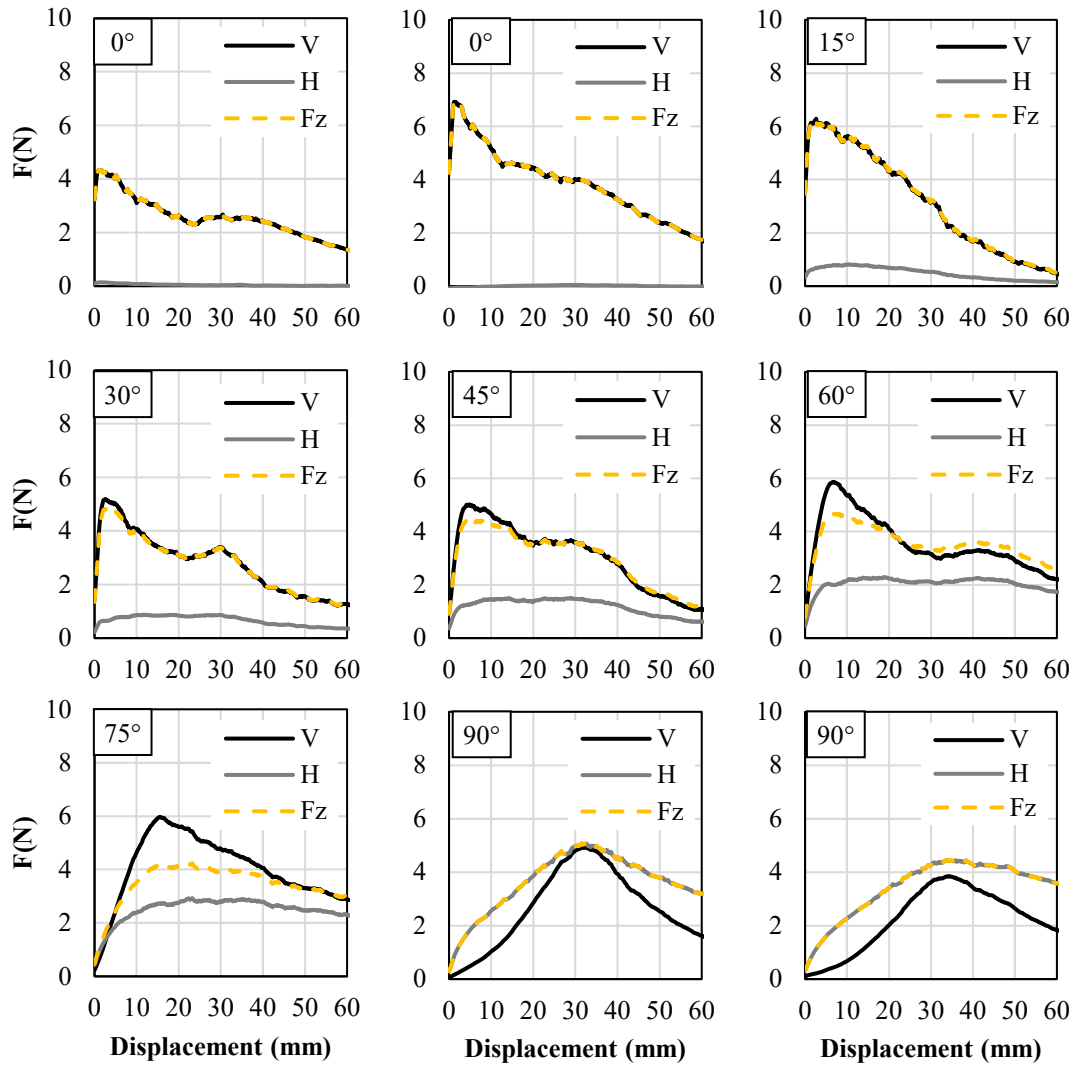


Figure 5.4: Force versus displacement for the 6-leg model showing force in the vertical-, horizontal-, and z-direction

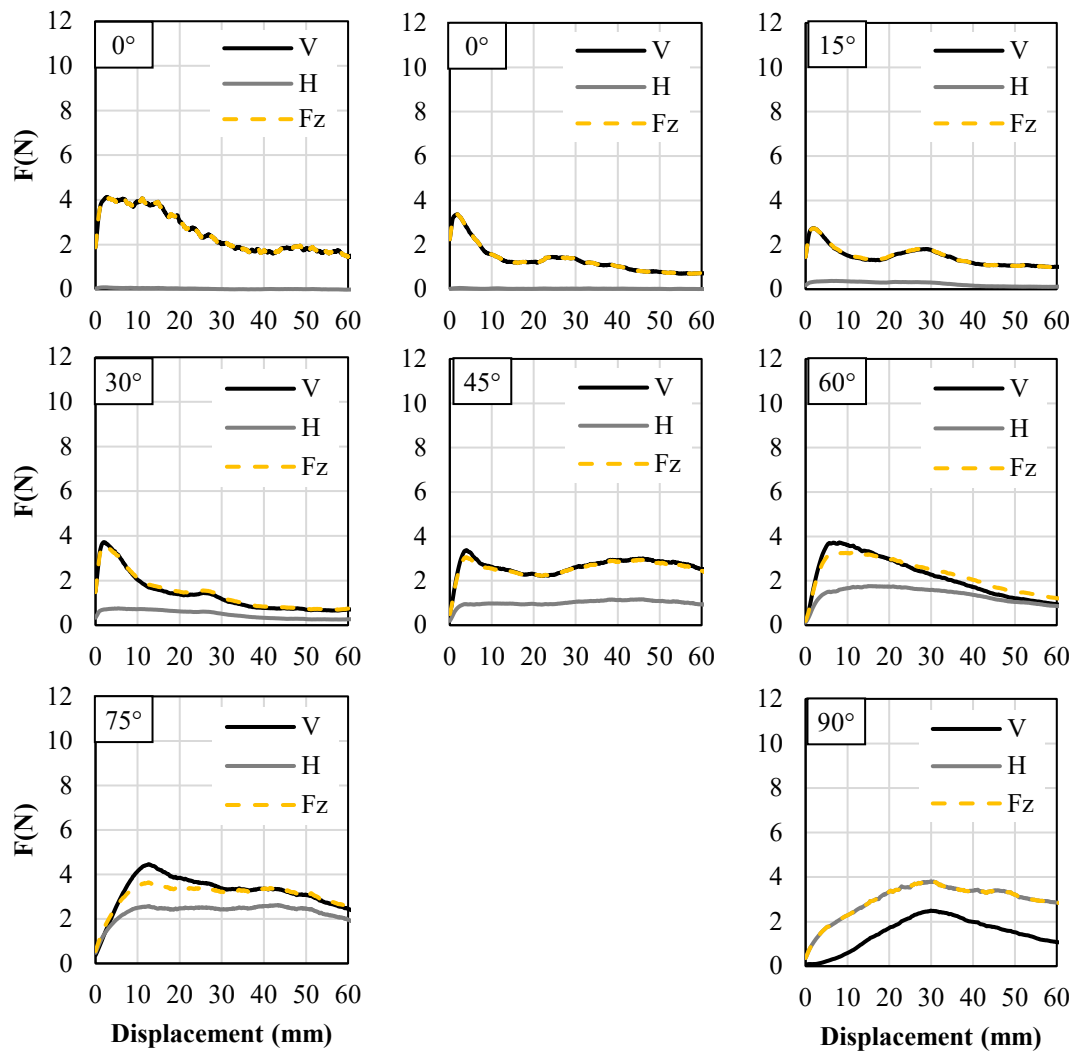


Figure 5.5: Force versus displacement for the 3-leg model showing force in the vertical-, horizontal-, and z-direction

### 5.1.3 Vertical vs. horizontal load

In showing the relationship between vertical and horizontal load, a failure envelope can be approximated. Dattola et al. (2020) have shown that analytical macroelement failure envelopes can be adapted to capture the combined loading behavior of small-scale root models. In

addition, the parabolic envelope proposed by Butterfield and Ticof (1979) and Gottardi and Butterfield (1993) for shallow foundations has been found by Jin et al. (2020) to capture the loads measured at failure in small-scale tests using a robotic arm. The equation for the Gottardi and Butterfield (1993) failure envelope is Equation 5.1.

$$H = \beta_1 V \left[ 1 - \left( \frac{V}{V_m} \right)^{\beta_2} \right] \quad 5.1$$

In Equation 5.1,  $H$  is the horizontal load,  $V$  is the vertical load,  $V_m$  is the maximum vertical capacity under vertical loading,  $\beta_1$  is equal to tangent of the interface friction angle of the sand (taken here as equal to the soil friction angle,  $\beta_1 = 0.67$ ), and  $\beta_2$  is a fitting parameter. This equation was developed for shallow foundations which have a null horizontal capacity when the vertical load is zero. This equation was thus adapted to allow for a non-zero horizontal capacity when  $V$  is zero as in Equation 5.2.

$$H = H^* + \beta_1 V \left[ 1 - \left( \frac{V}{V_m} \right)^{\beta_2} \right] \quad 5.2$$

In Equation 5.2,  $H^*$  is a fitting parameter that represents the horizontal capacity when the vertical capacity is zero. It is noted that this is a theoretical value, as the experimental results showed that the vertical load was never zero even during the pullout tests at  $90^\circ$ . When plotting the analytical failure envelopes in the subsequent section, engineering judgement is used to choose values for the  $\beta_2$  and  $H^*$  parameters.

The relationship between vertical and horizontal load for the pile model is shown in Figure 5.6. The  $0^\circ$  test for the pile model yielded unreliable results, as previously noted. The vertical force magnitude for the pile model was higher than the horizontal force magnitude for  $15^\circ$

through  $45^\circ$ , suggesting that at those angles, the vertical capacity was greater. At  $60^\circ$ , the vertical and horizontal load have a nearly 1:1 relationship at peak load. For angles  $75^\circ$  and  $90^\circ$ , the horizontal capacity is greater than the vertical force. The failure envelope in Figure 2.5 suggests the largest capacity was achieved at a pullout angle of  $90^\circ$  where the ratio of vertical to horizontal load was approximately 0.33. The latter four assessments align with the data in Figure 5.2. The plotted failure envelope clearly shows its asymmetric shape, with greater H capacities than V capacities for the  $90^\circ$  test. The  $\beta_2$  and  $H^*$  values used to determine the envelope were 20 and 2.6N, respectively.

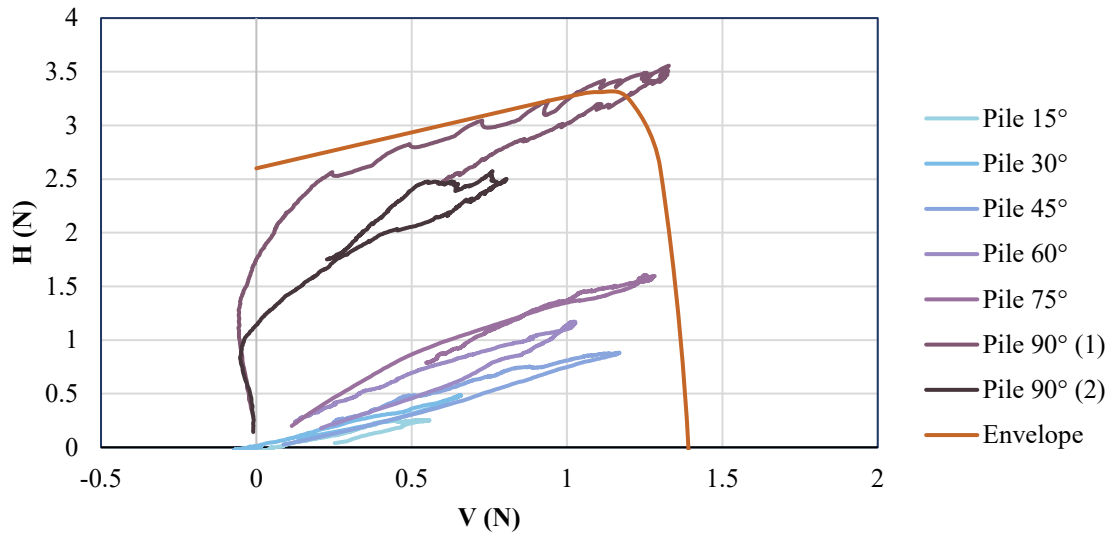


Figure 5.6: Vertical versus horizontal load for the pile model. Failure envelope is drawn in orange.

The relationship between vertical and horizontal load for the plate model is shown in Figure 5.7. As previously mentioned, the  $30^\circ$  test yielded inaccurate results and was removed from this analysis. The vertical capacity was greatest for the tests at  $0^\circ$  to  $75^\circ$ ; however, the horizontal capacity was greater for the  $90^\circ$  test. It is noted that considerable V forces were recorded during the  $90^\circ$  test, which involved a horizontal pullout. This is due to the plate at the

bottom of the anchor which causes the mobilization of vertical forces. The largest capacity was recorded in the 45° test where the ratio of vertical to horizontal load was approximately 4.6. The latter three assessments align with the data in Figure 5.3. The plotted analytical failure envelope is highly asymmetric, with greater vertical capacities than horizontal capacities. The envelope also suggests an interaction between the horizontal and vertical loading which results in the data of the 90° test closely following the envelope at vertical forces greater than 2 N. The  $\beta_2$  and  $H^*$  values used to determine the envelope were 4 and 3.3N, respectively.

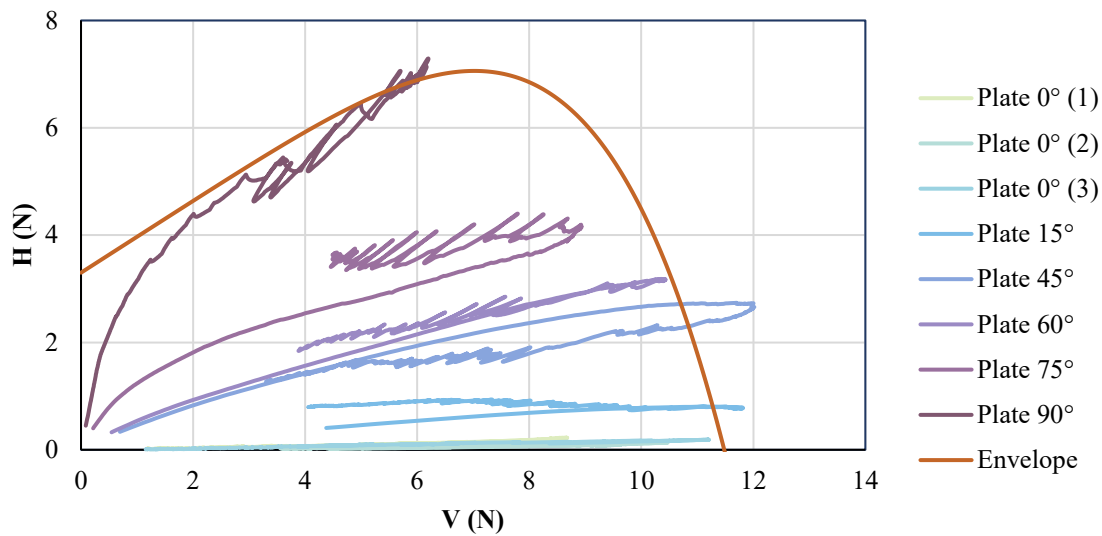


Figure 5.7: Vertical versus horizontal load for the plate model. Failure envelope is drawn in orange.

The relationship between the vertical and horizontal load for the 6-leg model is shown in Figure 5.8. The vertical capacity was greatest for tests at 0° to 75° while the horizontal capacity was greater for the test at 90°. The largest capacity was recorded in the 15° test where the ratio of vertical to horizontal load was approximately 8. The latter three assessments align with the data in Figure 5.4. The analytical failure envelope is more symmetric than that for the pile and

plate anchors. The  $\beta_2$  and  $H^*$  values used to determine the envelope were 5 and 2.5 N, respectively.

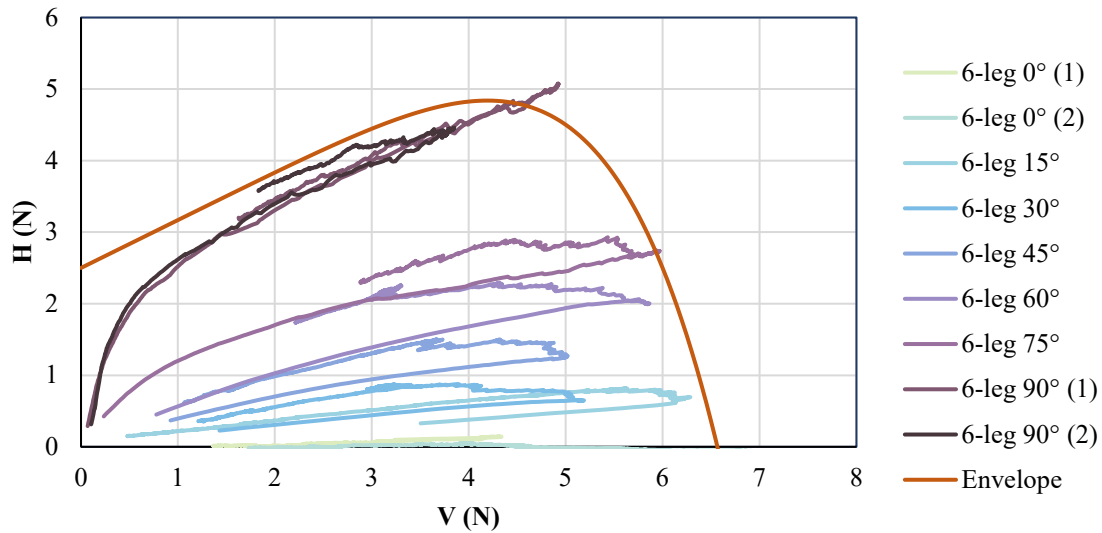


Figure 5.8: Vertical versus horizontal load for the 6-leg model. Failure envelope is drawn in orange.

The relationship between the vertical and horizontal load for the 3-leg model is shown in Figure 5.9. The vertical capacity was greatest for tests at  $0^\circ$  to  $75^\circ$  while the horizontal capacity was greatest for the  $90^\circ$  test. The largest capacity was recorded in the  $90^\circ$  test where the ratio of vertical to horizontal load was approximately 0.42. The latter three assessments align with the data in Figure 5.5. The plotted failure envelope is less symmetric than that for the 6-leg model, with greater horizontal capacities than vertical capacities. The  $\beta_2$  and  $H^*$  values used to determine the envelope were 6 and 2.2 N, respectively.

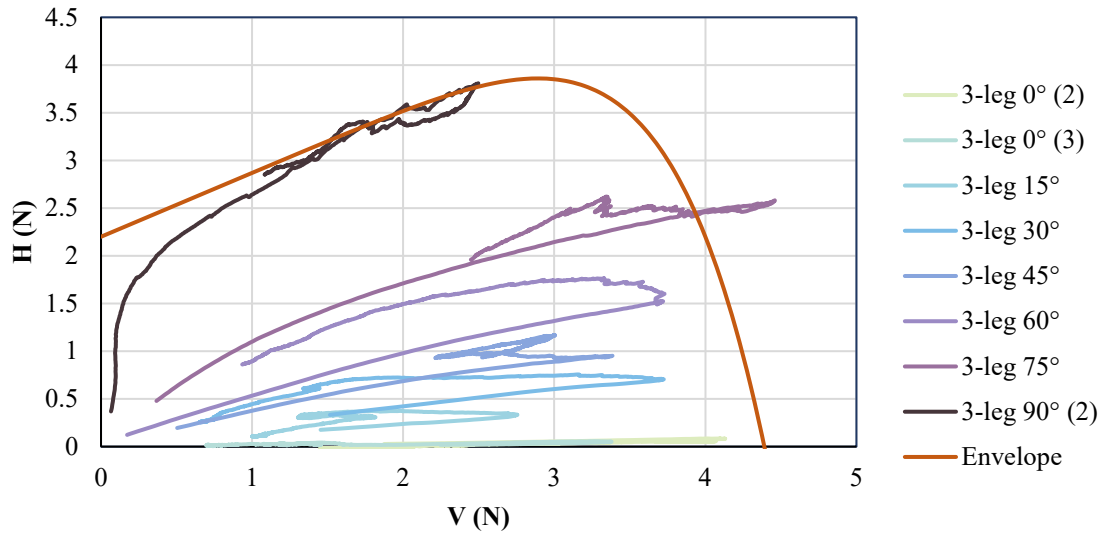


Figure 5.9: Vertical versus horizontal load for the 3-leg model. Failure envelope is drawn in orange.

The peak envelopes are shown on one plot in Figure 5.10.

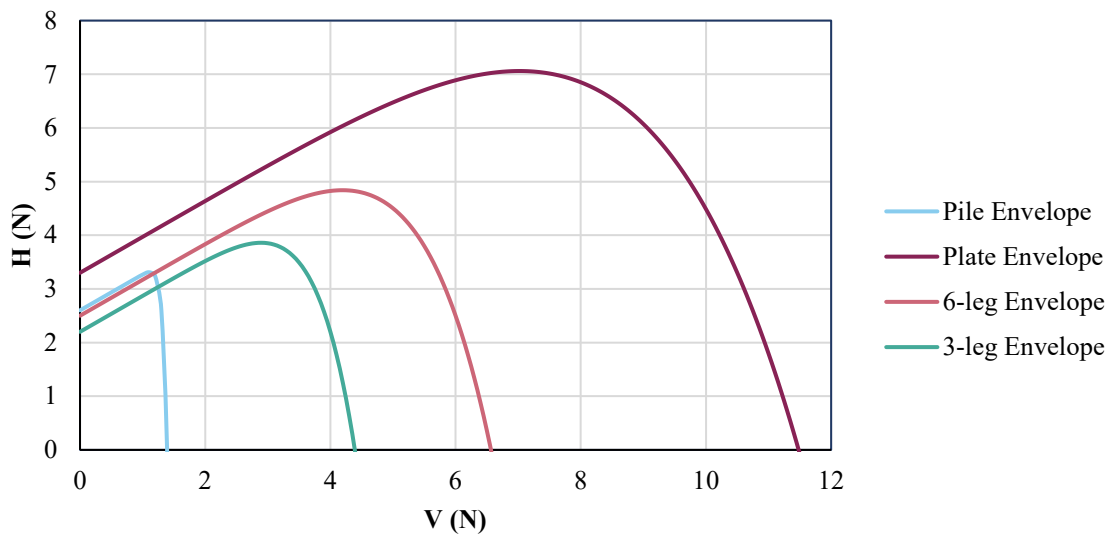


Figure 5.10: Failure envelopes for the four models

The plate model failure plane encompasses all other failure planes, implicating that the plate model carries the highest loads before failure. The pile has a larger failure plane than the 3-leg and the 6-leg model for vertical loads below approximately 1.2 N and then drops below all the

models at any loads higher than 1.2 N. This finding suggests that the pile model has high capacity for horizontal loads and performs on par with the 6-leg model in lateral loading conditions up to 1.2 N. The 6-leg model has a larger failure envelope than the 3-leg model. Because there are more legs and therefore more volume in the anchor, the 6-leg model will likely have a failure envelope that is more like the plate model's than the pile model's. Accordingly, the 3-leg model has less anchor volume and can be expected to have a failure envelope more like the pile model's than the plate model's.

#### **5.1.4 Peak loads**

The peak loads were determined after applying the moving average to the force data. The peak loads are shown for each model at all tested angles in the vertical-, horizontal-, resultant-, and z-directions in Figure 5.11. The resultant force is calculated using the vertical and horizontal loads in the Pythagorean Theorem and the pullout angle.

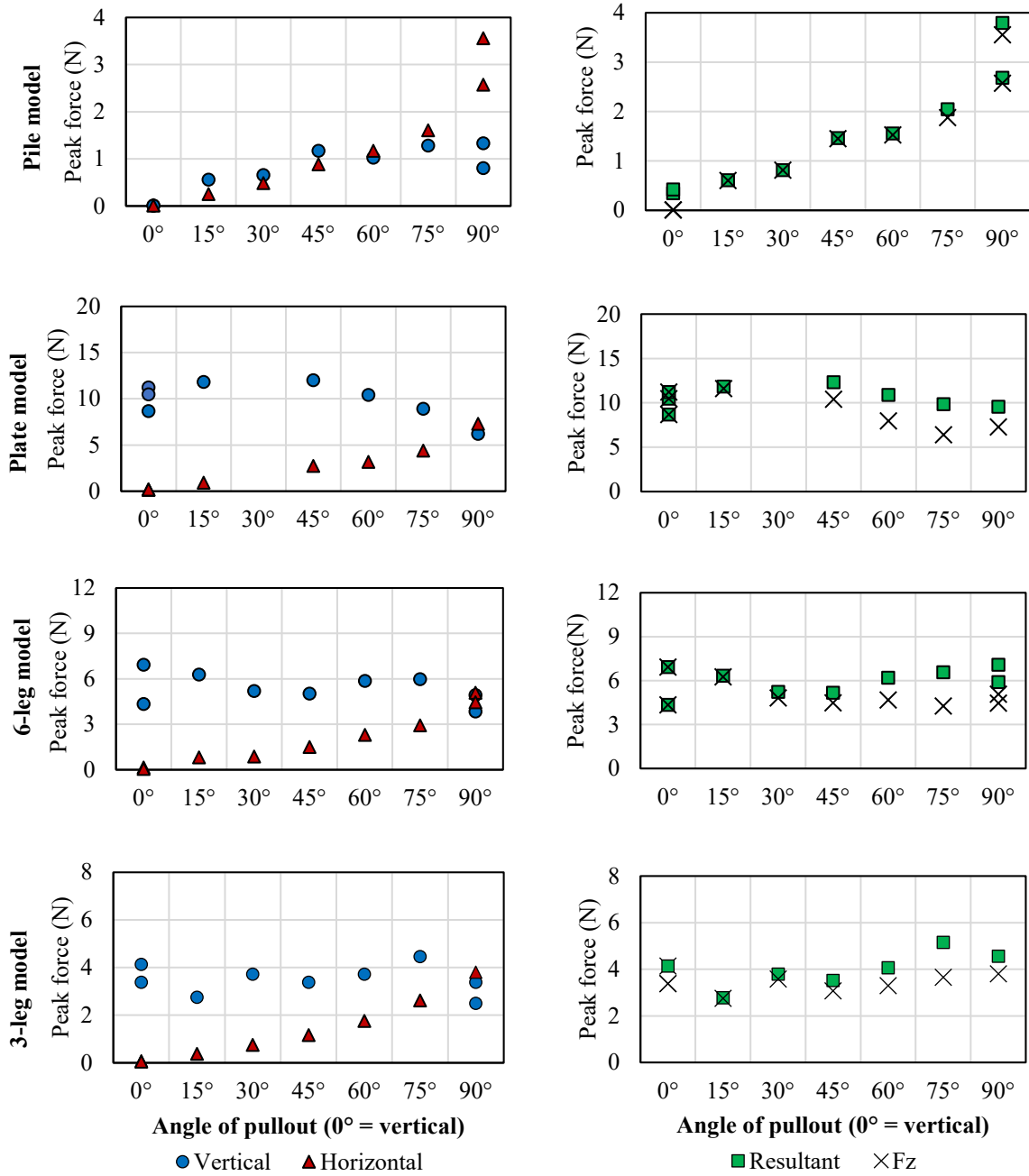


Figure 5.11: Peak force for each model in the vertical-, horizontal-, resultant-, and z-directions

#### 5.1.4.1 Pile

For the pile model, the peak load increases as the angle increases for all directions, with the only exception being a slight decrease in vertical peak loads after 45°. This general

upward trend can be attributed to the fact that a pile under vertical loading is mainly supported by shaft friction. The more horizontal the pile becomes, the more lateral earth pressure is assisting the capacity of the pile likely resulting in an increase in the radial stress acting against the pile wall. The vertical peak load is higher than the horizontal peak load for  $0^\circ$  to  $45^\circ$ . For  $60^\circ$  to  $90^\circ$ , the horizontal peak load is higher than the vertical peak load. The shift can be expected since the pullout direction is gradually becoming more horizontal. The resultant forces match the  $F_z$  for  $15^\circ$  to  $60^\circ$ . For all other angles, the resultant peaks are greater than  $F_z$  peaks. The horizontal load controls the resultant maximum peak load which occurs at  $90^\circ$  for the pile model.

#### 5.1.4.2 Plate

The plate model's vertical peak load increases slightly as the angle increases from  $0^\circ$  to  $15^\circ$ . After  $45^\circ$ , the peak load drops. The pattern of the vertical trend suggests that the plate model has peak vertical capacity when pulled out between  $15^\circ$  and  $45^\circ$ , likely due to an increase in the radial effective stresses acting against the wall of the anchor model. The lowest vertical capacity occurs at  $90^\circ$ . The vertical peaks are higher than the horizontal peaks except for the  $90^\circ$  test. The horizontal peak load increases as the angle increases from  $0^\circ$  to  $90^\circ$ . The resultant and  $F_z$  peaks indicate that the vertical capacity has a greater influence on the peak magnitudes, and the maximum resultant and  $F_z$  forces take place between  $15^\circ$  and  $45^\circ$ . The resultant and  $F_z$  nearly match for angles  $0^\circ$  and  $15^\circ$ . For all other angles, the resultant peaks are greater than  $F_z$  peaks. The vertical peak controls the peak resultant load which occurs between  $15^\circ$  and  $45^\circ$  for the plate model. Thus, the loading on the plate can be assumed as most optimal for anchorage within this pullout angle range.

#### 5.1.4.3 6-leg

The vertical peak loads for the 6-leg model exhibit a decrease as the angle increases from  $0^\circ$  to  $45^\circ$  then an increase as the angle increases from  $45^\circ$  to  $75^\circ$  and finally a decrease as the angle increases to  $90^\circ$ . Two local maxima occur at  $0^\circ$  and  $75^\circ$ , with the greatest peak load occurring at  $0^\circ$ . Two local minima occur at  $30^\circ$  and at  $90^\circ$ , with the lowest peak at  $90^\circ$ . The vertical peaks are always greater than the horizontal peaks except for at  $90^\circ$ . The horizontal peak forces increase as the angle increases from  $0^\circ$  to  $90^\circ$ . The resultant and Fz peaks nearly match at angles  $0^\circ$  and  $15^\circ$ . For all other angles, the resultant peaks are greater than Fz peaks.

The 6-leg model is similar to the plate model in shape except that there are cut-outs in the plate and the leftover stems have been rounded. Since the plate and pile are two extremes in geometry relative to the four geometries tested, the 6-leg model can be expected to behave like a combination of the pile and plate models. This, however, does not hold true. The 6-leg model experiences a minimum peak at  $30^\circ$ , whereas the plate likely experiences a peak at that angle. The 6-leg model also does not increase in peak values with increasing angle as the pile does. Instead, the data suggests that the 6-leg shape provides the most optimal capacity at both  $0^\circ$  and  $90^\circ$ . The six legs can help provide capacity from overburden stress during a vertical pullout. During a horizontal pullout, the model may behave more like a pile while the legs drag horizontally through the soil, providing little capacity to the system.

#### 5.1.4.4 3-leg

The vertical peak forces for the 3-leg model show no clear trend. The maximum peak occurs at 75° and the minimum peak occurs at 90°. The vertical peaks are greater than the horizontal peaks except at 90°. The horizontal peak loads increase with increasing angle. The resultant and Fz nearly match at 15° and 30°. For all other angles, the resultant peaks are greater than the Fz peaks. The resultant peak is highest at 90° which suggests that the horizontal peaks control.

The 3-leg model has less legs than the 6-leg model and will possibly behave more like a pile than the 6-leg model. This conjecture can be considered relatively true when assessing the data. The model has minimal change in peak resultant until the angle reaches 60° after which the peak values increase, similar to the pile. The greater peak forces relative to the pile for angles lower than 60° can be attributed to the presence of the three legs.

## 5.2 LOADING EFFICIENCY

The absolute values of the force measurements are useful for assessing the performance of each individual model. When comparing the performance of each model for the sake of assessing material efficiency, the data can be normalized by either mass or volume. Since the models were 3D-printed to the same density, the volume can be used to normalize the data.

### 5.2.1 Volume normalized peak load

Before comparing performance between models, the volume normalized peak loads for each model will be useful to analyze. The volumes of each model are in Table 5.2. When assessing the trends in Figure 5.12, the trends

**Table 5.2:** Model volumes

<b>Model</b>	<b>Volume (mm<sup>3</sup>)</b>
Pile	2062
Plate	8247
3-leg	3092
6-leg	4123

are nearly identical to those in Figure 5.11 because the volume remains fixed for each anchor model. The results are provided here for completeness.

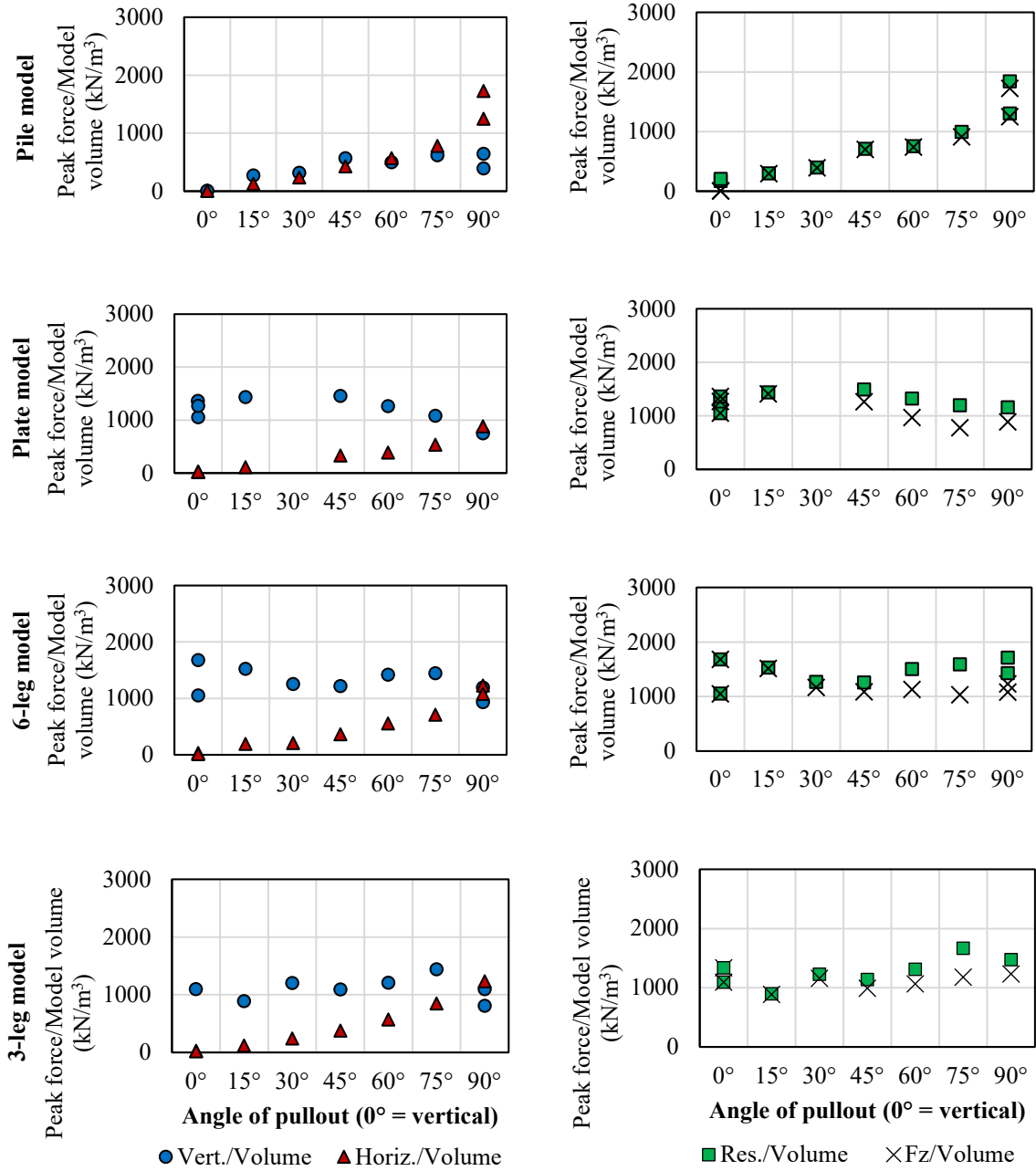


Figure 5.12: Volume normalized peaks for vertical-, horizontal-, resultant-, and z-direction for the tested models

## 5.2.2 Vertical capacity comparison

Isolating the vertical direction loading helps to understand the relationship between angle of pullout and directionality of loading.

### 5.2.2.1 Absolute capacity

The absolute capacity of the models in the vertical load direction are compared between models in Figure 5.13. Performance is measured by comparing peak forces, with the highest being the best performing. For all of the comparisons, the plate model outperforms all others, followed by the 6-leg, then the 3-leg, and the lowest being the pile. This trend can be attributed to the greater volume and surface area of the plate relative to the 6-leg, the 6-leg relative to the 3-leg, and the 3-leg relative to the pile. The end anchoring feature generally provides more capacity as it allows for mobilization of bearing resistances. This trend cannot be fully visualized for the 30° comparison since the plate model data was inaccurate.

### 5.2.2.2 Volume normalized capacity

After normalizing for volume, the relationship between the models for a given angle changed. The comparison for the normalized vertical peak loads is in Figure 5.14. At 0°, the plate model and 3-leg model yield similar normalized vertical forces. The 6-leg model performed worse than the plate and 3-leg for one test, but better than both for another test, suggesting some scatter in the data. The pile model's vertical force was negligible. At 15°, the order of vertical peak force from highest to lowest is the 6-leg, plate, 3-leg, and pile models. At 30° and 60°, the trend matches that at 15°, minus the fact that the plate model is missing from the 30° test. At 45°, the plate model outperforms the 6-leg model, followed

by the 3-leg and pile models. 6-leg and 3-leg models' peak vertical, normalized force at 75° are nearly identical, followed by the plate model then the pile model. At 90°, the 6-leg outperforms the 3-leg followed by the plate and the pile.

The intent of this comparison is to identify the material efficiency in pullout for the models tested. In normalizing the peak values, the effect of volume (proportional to the effect of mass) on the model's maximum capacity is removed, showing which model has the best material efficiency. For 0°, 15°, 30°, 60°, and 90°, the 6-leg model outperforms all other models. The 3-leg model performed similar to or worse than the plate model except for at 75° where the 3-leg model performed as well as the 6-leg model. The plate model and the 3-leg model therefore can be said to have similar material efficiency. This may be attributed to the 3-leg model's asymmetry or its lower volume. The suggestion from this comparison is that simplified tree root shapes can be more material efficient in carrying anchorage capacity than plate anchors and piles. More specifically, a 6-leg simplified tree root shape has a greater load capacity per volume in most load direction than a 3-leg shape, a plate, and a pile.

In Mallett (2019), the tests performed suggested that the normalized capacity of tree root shapes with an internal branching angle of 90° had the greatest capacity for the 3-leg model relative to the 6-leg model. The results of the work in this thesis suggest that the 6-leg model has a greater capacity than the 3-leg model. This difference may be the result of different experimental methods and different model geometries.

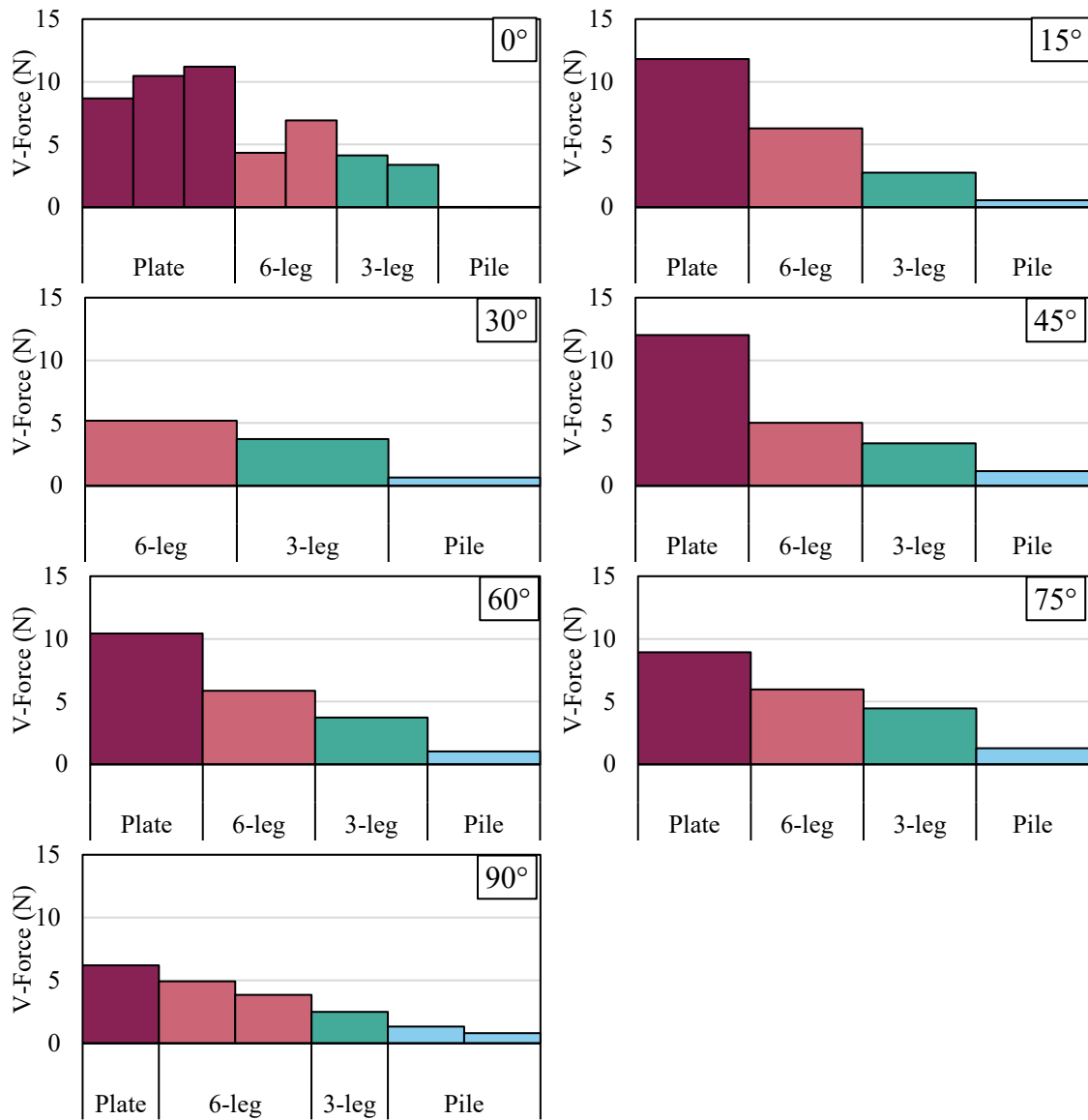


Figure 5.13: Vertical peak loads for each angle compared between models

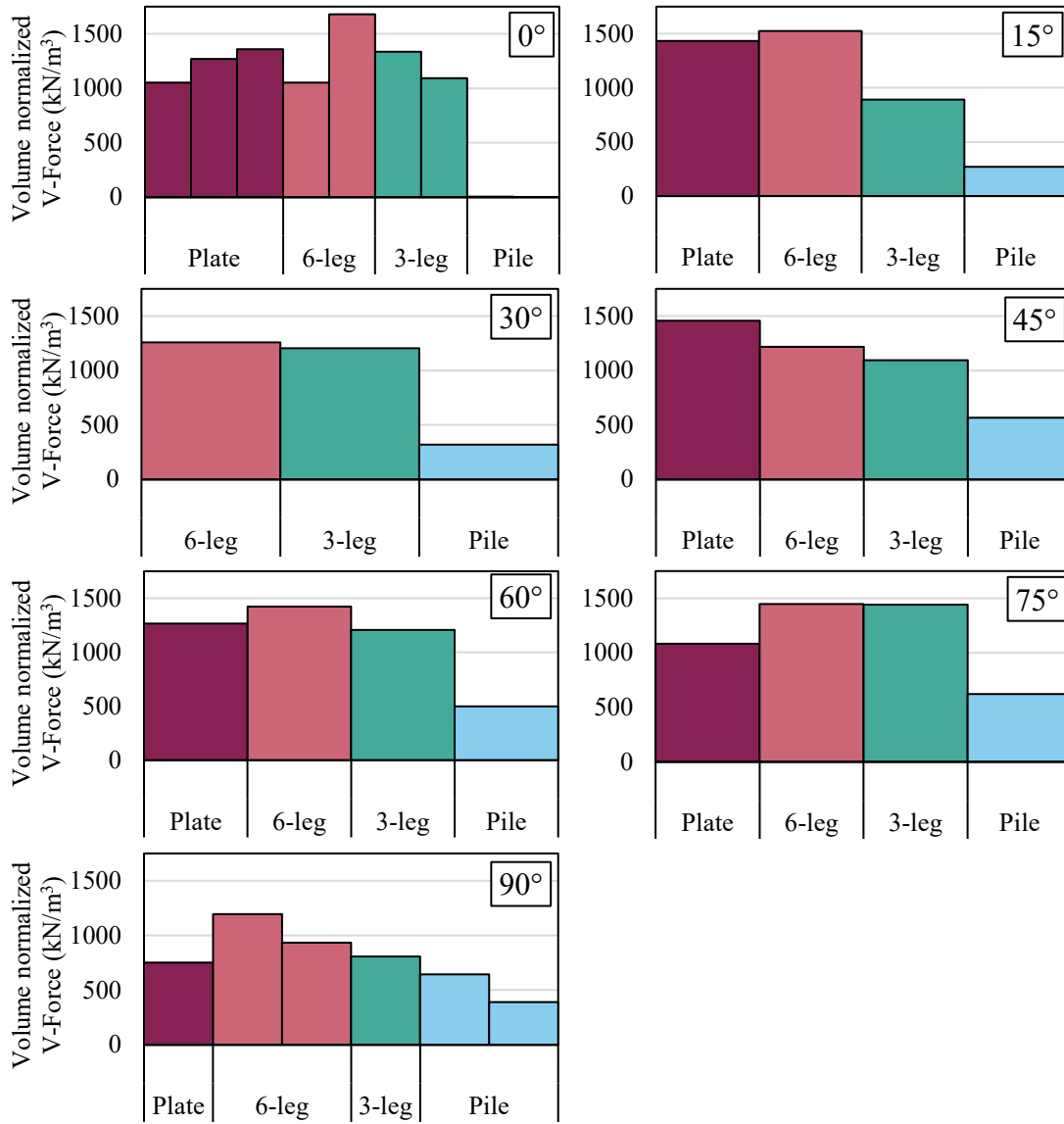


Figure 5.14: Vertical, volume normalized peak loads for each angle compared between models

### 5.2.3 Horizontal Capacity Comparison

Isolating the horizontal direction loading helps to understand the relationship between angle of pullout and directionality of loading.

#### 5.2.3.1 Absolute capacity

The absolute peak loads are shown in Figure 5.15. As for the vertical loading, the plate has a higher peak horizontal force than all other models, followed by the 6-leg model, the 3-leg model, then the pile. The reason for this order is as mentioned in Section 5.2.2.1.

#### 5.2.3.2 Volume normalized capacity

The normalized peak loads are shown in Figure 5.16. No particular trend occurs for every angle. At  $0^\circ$ , the 6-leg model has the highest peak, followed by a close tie between the plate model and the 3-leg model, with the pile performing the worst. At  $15^\circ$ , the 6-leg outperforms all others, while the three others are nearly the same. At  $30^\circ$ , each of the models perform similarly. At  $45^\circ$  and higher, a noticeable trend occurs showing that the 3-leg model and the pile perform best and perform similarly. The 6-leg follows behind, and the plate is the worst performing.

Similar trends are shown for  $60^\circ$ ,  $75^\circ$ , and  $90^\circ$ , where the 3-leg and pile models outperform the 6-leg model, and the plate consistently shows the smallest volume normalized horizontal force. The suggestion from this comparison is that 3-leg shape and pile shape are most advantageous in the horizontal loading direction. Since the 3-leg shape is closest to pile relative to the other two shapes, the similar performance between the two suggests that the pile shape gives the most advantage to the anchorage capacity. In some instances,

the 3-leg outperforms the pile, suggesting that the legs on the model add some leverage to the model during pullout, particularly at more shallow angles (e.g. 45° or greater).

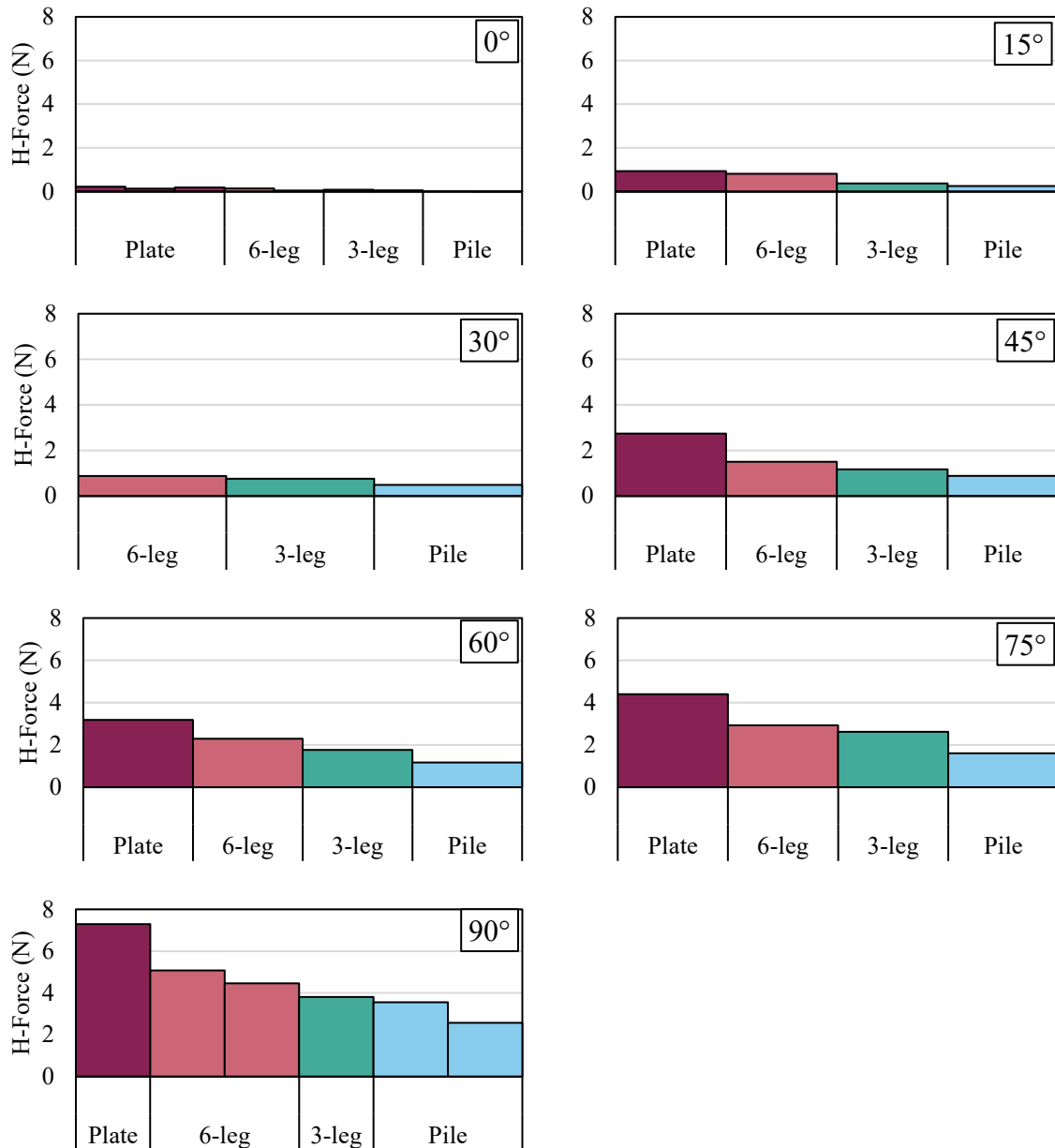


Figure 5.15: Horizontal peak loads for each angle compared between models

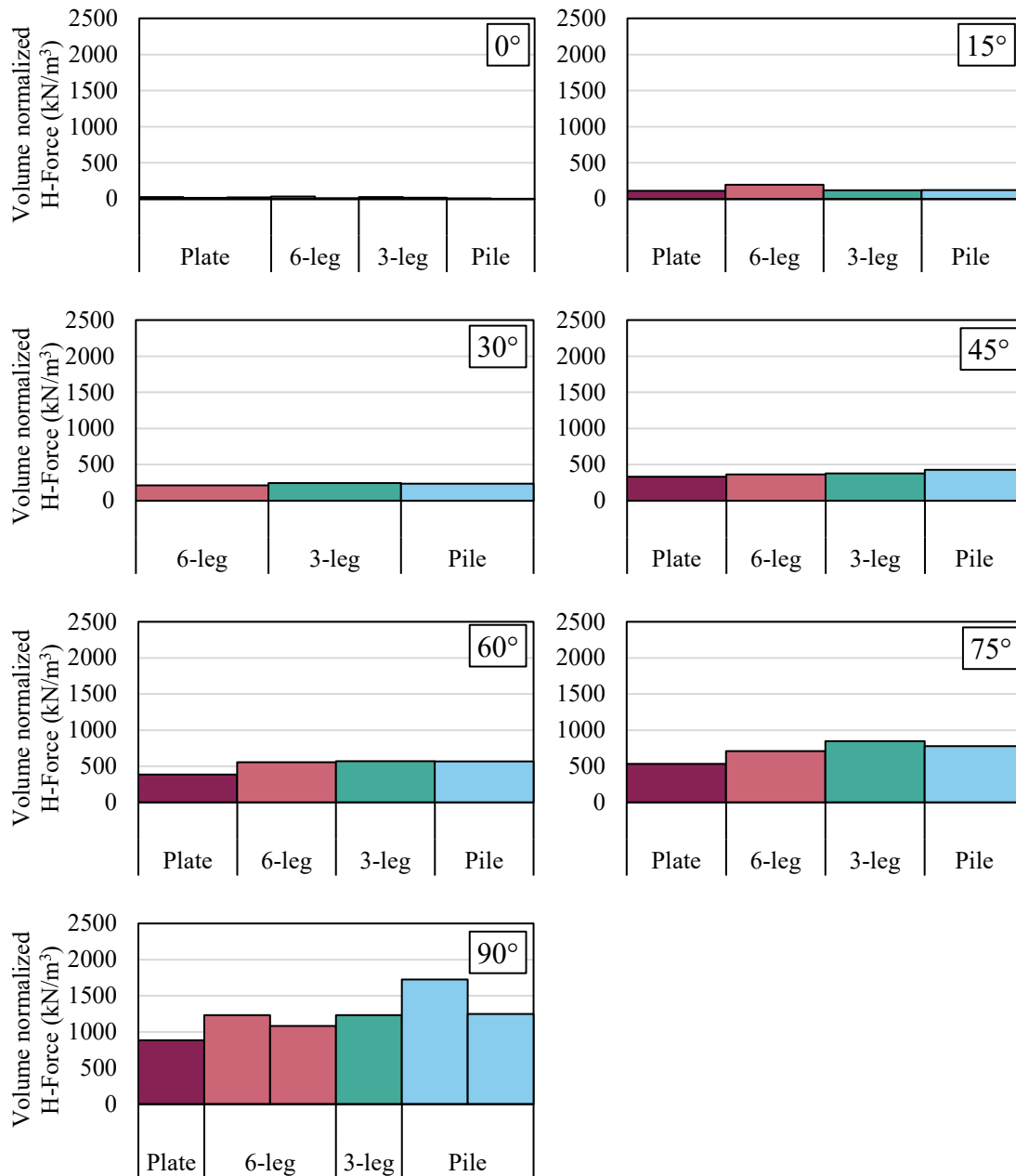


Figure 5.16: Horizontal, volume normalized peak loads for each angle compared between models

#### 5.2.4 Resultant capacity comparison

The resultant of the calculated vertical and horizontal components and the volume-normalized resultant are compared between models in Figure 5.17 and Figure 5.18, respectively. The trends for both sets of plots closely follow the trends from the vertical component of force. The resultant information deviates from the trends of the vertical force component when observing the normalized force at 75° and at 90°. For the vertical force at 75°, the 6-leg model has a higher normalized peak load than the 3-leg model. The reverse is true for the resultant force, where the 3-leg is higher. This trend can be noted in the horizontal force direction for the given angle. The vertical force at 90° shows that 6-leg has the highest normalized peak load of the models. The resultant force shows a narrow window of difference between the 6-leg model peak and the pile peak.

These trends indicate that the peak load is governed by the vertical load performance until more shallow angles are tested. At shallower angles, the horizontal capacity contributes to the peak load behavior. The results also indicate that the material efficiency of the plate anchor decreases as the loading angle is increased (i.e. becomes more horizontal). The opposite trend is true for the pile model, where the material efficiency increases as the loading angle is increased.

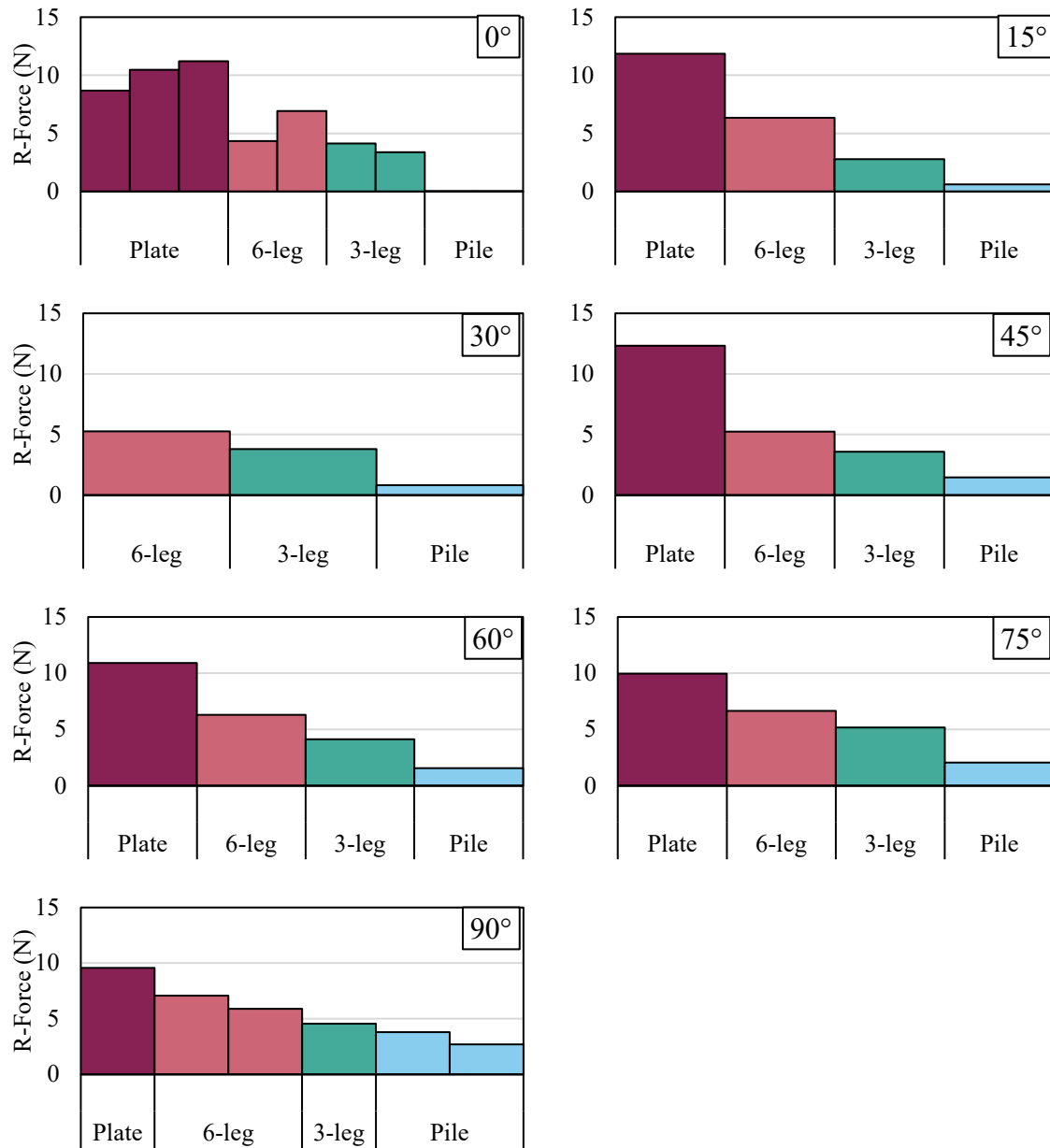


Figure 5.17: Resultant peak loads for each angle compared between models

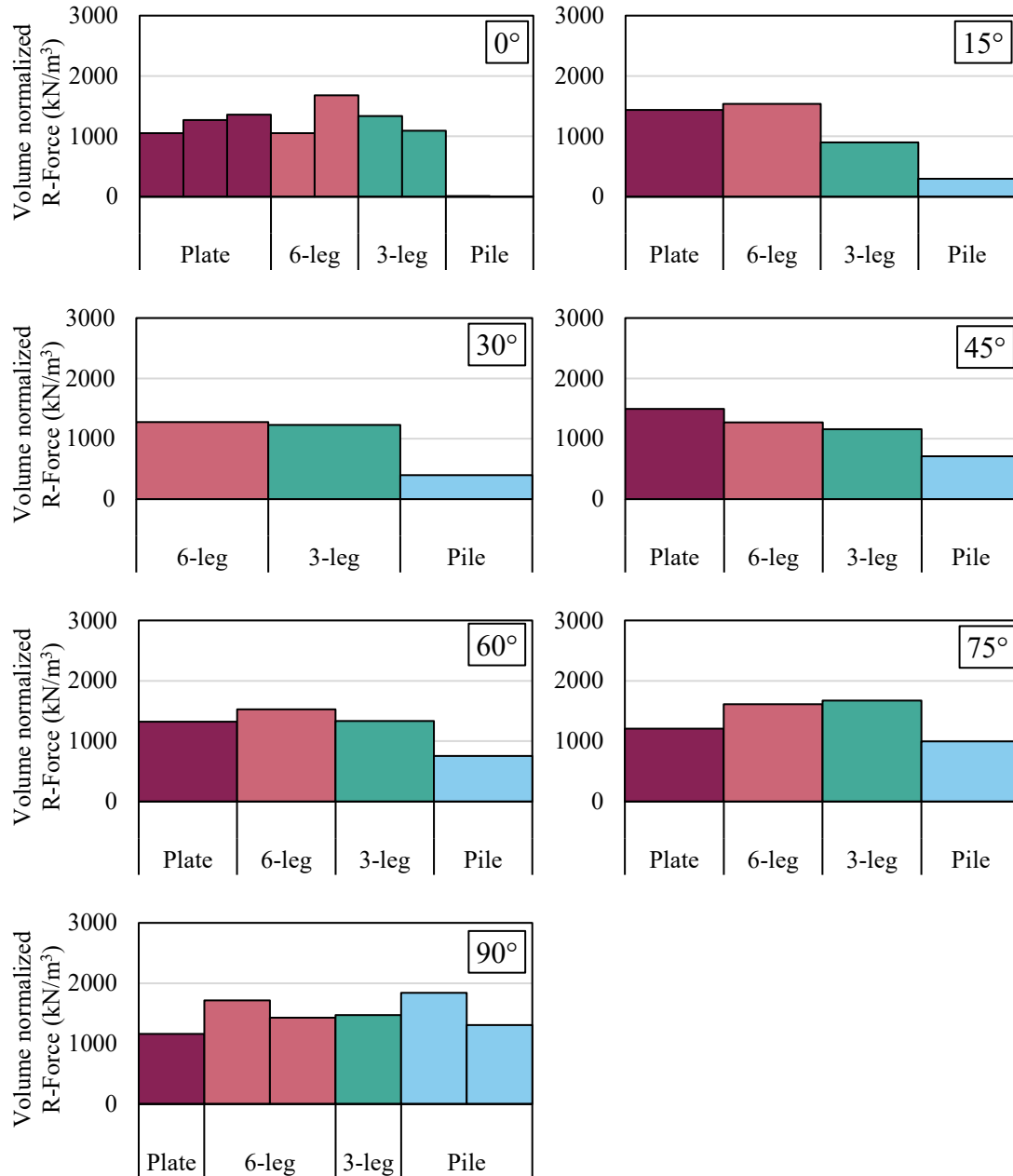


Figure 5.18: Resultant, volume normalized peak loads for each angle compared between models

## CHAPTER 6 CONCLUSIONS

A core conjecture in bio-inspiration is that natural processes may be more material efficient because they were developed in conditions with limited resource availability. Existing literature indicates that tree roots are designed in part for nutrient intake and in part for anchorage. The anchorage of tree root depends on many factors, such as tree root type, tree root architecture, and tree root material. Tree root architecture and its relation to pullout capacity is widely studied and foundational to the work in this thesis. Bio-inspiration yields the hypothesis that tree roots can be material efficient (i.e. capacity per material unit volume).

Tree root systems typically have complex geometries. To enable study of the effects of root architecture on anchor capacity, a 3D-printer was used to generate simplified model anchors. The Ultimaker S5 is a dual extrusion, Fusion Deposition Modeling (FDM) 3D printer. With its ability to print water soluble supports, complex models become easier to print since supports can be removed without leaving marks, residue, or filament globs on the surface of the print. The models were printed using Ultimaker Tough PLA, a material with moderate strength and mild flexibility. The four models selected for testing are a pile, a plate anchor, a 6-leg simplified tree root model, and a 3-leg simplified tree root model. All models were embedded in the soil 105 millimeters.

To test these models under the action of multi-directional loading, a force and torque sensor had to be applied on equipment that could move the models on a slow, precise path from a variety of angles other than vertical. The UR16e robotic arm was selected for this use. The UR16e robotic arm allows for six degrees of freedom. The arm has a built in F/T (force/torque) sensor, but the resolution of the sensor was not high enough to obtain valuable information from the tests. An external six-axis load cell was mounted to the tool end of the robot, called the Axia80-m20 F/T sensor. This load cell gave precise measurements that could detect the small loads in the tests

performed. The combination of the robotic arm and the load cell allowed for tests to be performed at low confining pressures for angles  $0^\circ$ ,  $15^\circ$ ,  $30^\circ$ ,  $45^\circ$ ,  $60^\circ$ ,  $75^\circ$ , and  $90^\circ$  while the three force and torque components were measured.

The anchor load tests were performed in a small cylinder with Ottawa F65 pluviated over the model. At least one test was performed for every model at every angle. All models exhibited the same behavior when transitioning from more vertical to more horizontal angles. The peak load was achieved at lower pullout displacements for more vertical angles and started occurring later in the test at higher pullout displacements for more horizontal angles. Before normalizing for volume, the plate anchor typically mobilized the highest peak load in both the horizontal, vertical, and resultant directions. After normalizing by volume, the 6-leg model typically mobilized the highest peak/volume with the 3-leg model and the pile occasionally having the highest peak/volume for more horizontal angles. The data suggests that the 6-leg model was more material efficient in pullout than the other models tested. The results confirm the hypothesis that tree roots are more material efficient in anchorage because of their geometry. The results also justify the use of 3D-printed models and a robotic arm to perform 1g testing of the models. The 3D printing of the models helps to quickly create complex structures with nearly identical material properties without having to outsource the model-making process. The six-axis readings from the robotic arm allows for the reading and analysis of combination loading, yielding behavior closer to that in the field (e.g multi-directional wind load).

The results of this work implore further testing of simplified tree root models. The work for this thesis was performed at 1g, leaving the possibility that further testing can be done in a geotechnical centrifuge or in the field to verify the trends at greater overburden pressures. Different root geometries can be tested to assess which root geometry is optimal for anchorage. Roots can also

be tested for their bearing capacity by pushing the models into the soil versus pulling them out. The potential for further research on this topic is abundant and well-justified by the work of this research and of others.

**REFERENCES**

- Bouma, T. J., Nielsen, K. L., Van Hal, J., & Koutstaal, B. (2001). Root system topology and diameter distribution of species from habitats differing in inundation frequency. *Functional Ecology*, *15*, 360-369.
- Butterfield, R., & Ticof, J. (1979). Discussion: Design parameters for granular soils. *Pro. 7th European Conf. on Soil Mech. Fndn Engng*, *4*, pp. 259-262. Brighton.
- Coutts, M. (1983). Root architecture and tree stability. *Plant and Soil*, 171-188.
- Coutts, M. (1989). Factors affecting the direction of growth of tree roots. *Annals of Forest Science*, 277-287.
- Datolla, G., Ciantia, M. S., Galli, A., Blyth, L., Zhang, X., Knappet, J. A., . . . Leung, A. K. (2020). A macroelement approach for the stability assessment of trees. *Geotechnical Research for Land Protection and Development*. Springer.
- Dyson, A. S., & Rognon, P. G. (2014). Pull-out capacity of tree root inspired anchors in shallow granular soils. *Geotechnique Letters*, *4*, 301-305. doi:10.1680/geolett.14.00061
- Ennos, A. R. (1989). The mechanics of anchorage in seedlings of sunflower, *Helianthus annuus* L. *New Phytologist*, *113*, 185-192.
- Fitter, A. H. (1987). An architectural approach to the comparative ecology of plant root systems. *New Phytologist*, *106*, 61-77.
- Fitter, A. H., Stickland, T. R., & Harvey, M. L. (1991). Architectural analysis of plant root systems, 1. Architectural correlates of exploitation efficiency. *New Phytologist*, *118*, 375-382.

- Fleming, K., Weltman, A., Randolph, M., & Elson, K. (2008). *Piling Engineering* (3rd ed.). Spon Press.
- Gottardi, G., & Butterfield, R. (1993). On the bearing capacity of surface footings on sand under general planar loads. *Soils and Foundations*, 33(3), 68-79.
- Gourvenec, S. (2007). Failure envelopes for offshore shallow foundations under general loading. *Geotechnique*, 57(9), 715-728. doi:10.1680/geot.2007.57.9.715
- Hamza, O., Bengough, A. G., Bransby, M. F., Davies, M. C., & Hallett, P. D. (2004). Mechanics of root-pullout from soil: A novel image and stress analysis procedure. *IOP Conference Series* (pp. 213-221). Yogyakarta, Central Java, Indonesia: Springer. doi:10.1007/978-1-4020-5593-5\_20
- Jin, Z., Shin, Z., & Hambleton, J. P. (2020). Small-scale Geotechnical Testing Using a Six-axis Robot. (No. 20-7/495S).
- Mallett, S. (2019). *Mechanical behavior of fibrous root-inspired anchorage systems*. Georgia Institute of Technology.
- Menashe, E. (2004). *The Tree and The Soil*. Retrieved from Greenbelt Consulting: <http://www.greenbeltconsulting.com/articles/treeandsoil.html>
- Mickovski, S. B., Benough, A. G., Bransby, M. F., Davis, M. R., & Hallett, P. D. (2007). Material stiffness, branching pattern and soil matric potential affect the pullout resistance of model root systems. *European Journal of Soil Science*, 58, 1471-1481. doi:10.1111/j.1365-2389.2007.00953.x

- Mickovski, S. B., Bransby, M. F., Bengough, A. G., Davies, M. R., & Hallett, P. D. (2010). Resistance of simple plant root systems to uplift loads. *Canadian Geotechnical Journal*, 47, 78-95. doi:10.1139/T09-076
- Palumbo, S. (2018). *Anisotropic Interface Shear Behavior of Granular Soil and Surfaces Biologically-Inspired by Snakeskin*. UC Davis.
- Perry, T. O. (1989). Tree Roots: Facts and Fallacies. *Arnoldia*, 49(4), 3-21.
- Schnelle, M. A., Feucht, J. R., & Klett, J. E. (1989). Root Systems of Trees - Facts and Fallacies. *Journal of Arboriculture*, 15(9), 201-205.
- Stokes, A., Ball, J., Fitter, A. H., Brain, P., & Coutts, M. P. (1996). An experimental investigation of the resistance of model root systems to uprooting. *Annals of Botany*, 78, 415-421. doi:0305-7364/96/100415+07 \$18.00/0